Probabilistic Engineering Mechanics 69 (2022) 103297

Contents lists available at ScienceDirect

Probabilistic Engineering Mechanics

journal homepage: www.elsevier.com/locate/probengmech

Characterization, propagation, and sensitivity analysis of uncertainties in the directed energy deposition process using a deep learning-based surrogate model

T.Q.D. Pham [a,c], T.V. Hoang [b], X.V. Tran [a,*], Seifallah Fetni [c], L. Duchêne [c], H.S. Tran [c], A.M. Habraken [c,d]

[a] Institute of Strategy Development, Thu Dau Mot University, 75100 Binh Duong Province, Viet Nam
[b] Chair of Mathematics for Uncertainty Quantification, RWTH-Aachen University, 52056 Aachen, Germany
[c] University of Liège, MSM Unit, Allée de la Découverte, 9 B52/3, B 4000 Liège, Belgium
[d] Fonds de la Recherche Scientifique de Belgique (F.R.S-FNRS), Belgium

ARTICLE INFO

Keywords:
Additive manufacturing
Uncertainty quantification
Sensitivity analysis
Monte-Carlo method
Melting pool sizes
Cooling rate

ABSTRACT

Uncertainties raised from process parameters, material properties, and environmental conditions significantly impact the quality of the printed parts in the directed energy deposition (DED) process. In this study, we perform the characterization, propagation, and sensitivity analysis of the uncertainties in the DED process using deep learning (DL)-based surrogate model to investigate the influence of the uncertain input parameters on the quality of the final printed product. A DL-based surrogate model is first constructed using the offline data obtained from a finite element (FE) model, which was validated against experiments. Sources of uncertainties are characterized using the probabilistic method and are propagated using the Monte-Carlo (MC) simulation. Moreover, we perform the sensitivity analysis (SA) to determine the most influential sources of uncertainty and two potential use cases based on uncertainty quantification results Owing to the fast execution time of the surrogate model, the MC simulation is significantly efficient in terms of computational resources as compared to the simulation that is solely based on the FE model. It is shown that the investigated sources of uncertainty contribute substantially to the inconsistency of the final product quality as they induce variations in temperature field, cooling rate at the liquidus point, and melting pool sizes. These quantities are also strongly dependent on the clad height. Based on the SA results, the laser power, the scanning speed, the heat convection, and the thermal conductivity induce the most uncertainties to the melting pool sizes. Two potential use cases are assessed to further demonstrate the usefulness of UQ results (i.e., uncertainty reduction). In general, these findings provide valuable insights for the process parameter optimization of the DED under uncertainty to improve the quality of the final printed parts.

1. Introduction

Additive Manufacturing (AM) technology is a unique capability for building complex three-dimensional (3D) objects from computer-aided design models. Among many technologies used for metallic AM, directed energy deposition (DED) is a flexible process adapted to repair components that failed during operations [1,2]. This method involves the deposition of metallic powder, which is melted via a focused heat source. DED is becoming widely used in industries to fabricate metal components in many applications such as equipment design [3,4] and robotics [5–7].

Despite many intriguing features, the main challenges limiting a wide adoption of DED process in industries are the sensitivity and inconsistency of the quality of the printed products on the manufacturing conditions [1]. During DED process, many physical phenomena occur in a short period and at the temperature above the melting, for instance, complex heat transfer behaviour and liquid–solid transformation of materials. In addition, multiple and complex temperature cycles generate heterogeneous microstructures [1,2]. Moreover, DED process inherently includes multiple uncertainty sources, such as input materials, powder quality, process parameters, environmental conditions, etc., which all can contribute to the inconsistency of the quality of fabricated products [8,9]. Consequently, tuning manufacturing parameters using experiments is an ad-hoc and time-consuming task that strongly depends on an expensive trial and error approach [8,10].

An efficient way to resolve the aforementioned problem is to use uncertainty quantification (UQ) during DED process [8,10–13]. The

* Corresponding author.
E-mail address: xuantv@tdmu.edu.vn (X.V. Tran).

https://doi.org/10.1016/j.probengmech.2022.103297
Received 3 December 2021; Received in revised form 28 April 2022; Accepted 8 May 2022
Available online 17 May 2022

UQ involves using mathematical methods to characterize the uncertain features associated with the DED process model (i.e., process parameters, material properties, and boundary conditions) as one or more random variables or random fields [14,15]. The input uncertainty is then propagated to the output — the Quantity of Interest (QoI). Finally, an optimization formulation that accounts for uncertainty, i.e., Bayesian inference or robust optimization methods, is applied to optimize the process parameters. However, a massive number of input–output pairs will be required in the propagation and optimization steps [15]. Using numerous experiments to obtain these pairs is impractically expensive. Therefore, finite element (FE) simulations of the manufacturing processes [10] which have a high predictive capability are usually employed to replace the experiments. Still, these numerical models could also be computationally expensive as one simulation to produce one input–output pair will take a few hours to a few days [10,15] and about a million input–output pairs are required in the Monte-Carlo (MC) simulations. Hence, a more efficient numerical approach is needed. Deep Learning (DL) appears to be a promising tool to build a surrogate model representing the relations between the quality indicators of fabricated products and the manufacturing process parameters [10,16–18] to replace the numerical simulations. Thanks to the trained DL models, the relations between process parameters and quality of printed pieces can be achieved with a significantly reduced computational time, providing an efficient tool for the optimization of the DED process parameters under uncertainty.

Currently, UQ studies [10,13,19,20] in AM fields are mainly focused on the laser powder bed fusion (L-PBF) process [10,19]. Tapia et al. [20] employed a UQ framework to account for uncertainties in process parameters and quantified their influences on the melting pool width. Lopez et al. [19] also performed a UQ to identify uncertainty in L-PBF models and concluded that the four popular sources of uncertainty in L-PBF are modelling assumptions, unknown simulation parameters, numerical approximations, and measurement errors. Besides, Wang et al. [10] performed an inverse UQ to calibrate and improve the 3D melt pool surrogate model using the Bayesian method. In addition, as mentioned in the U.S. Department of Energy office's manual report on energy efficiency and renewable energy, an integrated modelling approach with UQ is necessary to design and quantify advanced manufacturing processes in their long-term ten-year vision [21].

Even though UQ is crucial for achieving quality control, UQ in AM fields, particularly for DED process, is still at its early stage [11,12]. The above-mentioned studies are mainly focused on the L-PBF process and focused mainly on the process parameters [10,19]. This limited focus may result in excessive material wastage, time-consuming, and delay in the product development cycle since the material properties and the environmental conditions are not well investigated nor understood. Moreover, they considered the final melting pool as the QoIs while the evolution of the melting pool during the DED printing of layers, the temperature field, and the cooling rate, appear to strongly affect the homogeneity of the final microstructure [1,2]. This study aims to perform a systematic UQ in DED process to quantify the effects of uncertainties on the temperature field, cooling rate, and melting pool sizes. We also construct a DL-based surrogate model to accelerate the UQ process while still ensuring the acceptable statistical error. Moreover, we employ sensitivity analysis (SA) and some potential use cases interpreted from the UQ to identify which input uncertain parameters and their associated physical phenomenon significantly induce uncertainty in the final fabricated product.

The contribution of this work is summarized as follows. Firstly, instead of using the high-fidelity FE model, we construct a simple feed-forward neural network (FFNN)-based surrogate model to accelerate the UQ study. The FFNN hyperparameters are optimized using the data obtained from the FE simulations. Secondly, we investigate the effects of uncertainties raised from the process parameters, material properties, and environmental conditions on the temperature field, cooling rate, and melting pool sizes because they are intimately associated with various properties of the fabricated DED parts [1,2,22]. For instance, the melting pool sizes induce a nearby steep thermal gradient, which controls the thermal-gradient-dependent grain growth, the columnar microstructure development, and the defect formation within DED parts [2,22]. Thirdly, we carry out the SA analysis using the variance-based method [23] to identify which input uncertain parameters are significantly influential in inducing uncertainty in the QoIs. This task plays a vital role in process optimization since the parameters that caused the most uncertainty in the printed product can be recognized. Finally, we present two potential use cases (i.e., uncertainty reduction of cooling rate and melting pool depth) to further demonstrate the usefulness of the results obtained from the UQ.

This paper is organized as follows. The UQ methodology is developed in three sections as shown in Fig. 1: (i) the characterization of uncertain sources in DED process are described in Section 2, (ii) the uncertainty propagation using MC simulation accelerated by the DL-based surrogate model is introduced in Section 3, and (iii) the SA using variance-based method is summarized in Section 4. Finally, in Section 5, the key obtained results, which are the verification of the DL-based surrogate model, uncertainty propagation, sensitivity analysis, and two potential use cases based on UQ results, are discussed before the conclusion section.

2. Characterization of uncertain sources in DED process

This section investigates the physics of DED process, particularly identifies and characterizes the inherited uncertain sources (first step of the methodology illustrated in Fig. 1).

2.1. Physics of DED process

DED is an additive manufacturing processing technique involving very fast cooling rates for laser and electron beam energy sources [1,2]. During DED, many physical phenomena occur in a short period and at the temperature above the melting temperature of the powder, for instance, complex heat transfer behaviour and liquid–solid transformation of materials. Therefore, a diverging set of processing parameters coupled with the complex material properties and environmental conditions, including conduction, convection, and radiation emissivity, lead to difficulty in controlling the consistency of the final DED fabricated products.

An accurate model of the DED process is crucial to achieving quality control. Therefore, it should consider the transient temperature, and heat flow, complex transport phenomena, heating and cooling cycles as they strongly affect the microstructures of the printed sample. The temperature field (T) in the clad and the substrate is computed based on the classical heat transfer equation [24,25] as:

$$k\left(\boldsymbol{\nabla}^2 T\right) + Q_{\text{int}} = \rho C_p \frac{\partial T}{\partial t}, \tag{1}$$

where k is the thermal conductivity [W/m K], Q_{int} [W/m^3] is the density of power generated per volume in the workpiece, ρ [g cm^{-3}] is the material density, C_p [J/g K] is the apparent heat capacity, and t [s] is the time.

The following equation considers surface heat exchanges by convection, radiation emissivity and laser input energy generating a local surface flow [24,25]:

$$k\left(\boldsymbol{\nabla} T \cdot \mathbf{n}\right) = h\left(T - T_0\right) + \varepsilon\sigma\left(T^4 - T_0^4\right) + Q_{\text{laser}}, \tag{2}$$

where h [W/m^2 K] is the convective heat transfer coefficient, ε is the emissivity coefficient, σ [W/m^2 K^4] is the Stefan–Boltzmann constant, T_0 is the ambient temperature, and Q_{laser} [W/m^2] is the laser input energy.

In this study, the DED experiment of a bulk sample of M4 High-Speed Steel (HSS) [2] is considered for demonstration of the proposed UQ framework. A validated two-dimensional (2D) FE model of the

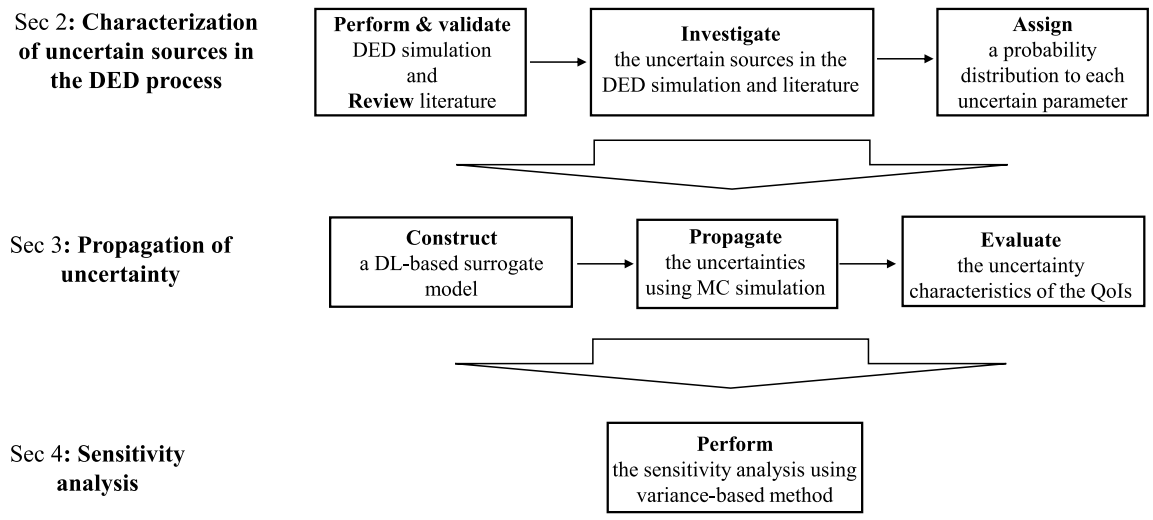

Fig. 1. The overview of UQ methodology including the characterization of the uncertain sources in DED process, propagation of uncertainty, and sensitivity analysis.

process has been developed by the authors in a previous work [2], described in detail in Appendix A. Fig. 2(a) shows a typical temperature field and melting pool sizes, the temporospatial temperature field at a random point, and the cooling rate at the liquidus point obtained by the FE model explained in Appendix A. This study chooses the temperature field, cooling rate, and melting pool sizes as the QoIs because they play an essential role in controlling microstructure formation during DED. Understanding the influence of the uncertainties on these QoIs can help to better understand the microstructures of each clad point and the potential defect generation, such as pores [1,2,7,24,25], which are key to understand the parameters affecting the most the final printed products.

2.2. Uncertain sources in DED process

Due to the complexity of DED process, several parameters influence the quality of the final product and can be considered uncertain sources [10–13]. In this study, based on the literature review and our experiences, we categorize these uncertainties into three classes as (i) process parameters, (ii) material properties, and (iii) environmental conditions [10–13]. Hereafter, we characterize the uncertainties from these three classes.

2.2.1. Uncertain sources in process parameters

Process parameters are the ones associated with the manufacturing system. Due to their temporal fluctuations and variations, there are uncertainties in these parameters, which strongly influence the quality of the final fabricated product, as pointed out by [9] (focused on the L-PBF process). In this DED study, four process parameters are considered: laser power, scanning speed, ambient temperature, and substrate preheating temperature. They are explained as below:

(i) *Laser power*: Laser power is one of the most critical parameters that affect the final fabricated product because it represents the primary heat sources of the printing system [9].
Uncertainty in the laser power emerges from inherent drift in the control system [24,25], heating of optics [9], and soot on optics [9]. Besides, the build chamber gets dirty during the DED process, and the laser path can be blocked because the soot accumulates beam delivery optics [9]. Consequently, this contamination effectively reduces the laser power. Some perturbation during the melting process can be observed and steady melt pool dimensions could not be achieved [26,27].
In this paper, the value of the effective laser input energy Q_{laser} is in the range of [0.97, 1.03] $\times Q_0$, where $Q_0 = 31158$ is the reference value (see Appendix A). In Section 2.3, we present the uncertainty of Q_{laser} by modelling the ratio $\mathcal{P} = Q_{\text{laser}}/Q_0$ as a uniform random variable bounded by $[0.97, 1.03]$.

(ii) *Scanning speed*: Scanning speed is the velocity of the laser head during the printing process. Along with the laser power, the scanning speed is another critical controllable parameter that influences the quality of the final fabricated product, evidenced in several articles [28–30].
Uncertainty in scanning speed emerges from inherent drift and intrinsic error [29,30] and heating and inherent errors in positioning optics [29,30]. Slight variations in scanning speed perturb the melting process and result in a noticeable effect on peak temperature and melt pool geometry [28]. In this paper, the value of scanning speed is assumed in the range of $v \in [335, 365]$ mm/ min, i.e., $v/v_{\text{ref}} \in [0.97, 1.03]$, where $v_{\text{ref}} = 350$ mm/ min.

(iii) *Ambient temperature*: As the material powder is involved during printing, its initial temperature affects the final temperature at the end of the printing process [31,32]. The ambient temperature is normally not considered as an input uncertain parameter from an industry viewpoint since the 3D printers are often located in an air-conditioned room. However, the thermal sensors used to adjust the ambient temperature are unstable with high temperatures [31] since the sensor body may struggle to dissipate heat in a heated environment. Therefore, we also consider the ambient preheating temperature as an input uncertain parameter in this study. In this paper, the value of ambient preheating temperature is assumed in the range of $T_a \in [284.15, 312.15]$ K, i.e., $T_a/T_{\text{a,ref}} \in [0.97, 1.03]$, where $T_{\text{a,ref}} = 293.15$ K.

(iv) *Substrate preheating temperature:* The substrate preheating temperature plays a vital role in avoiding the early crack during the printing process since it helps to reduce the temperature gradient between the clad and the substrate, resulting in lower internal stresses [33]. Also, it can make the temperature distribution more homogeneous, which helps to obtain a stable and stationary melt pool as a crack transmits the temperature differently from a continuous medium.
Uncertainty in the substrate preheating temperature arises from heating device errors, instability of heating sensors, and post-treatment errors [34,35]. In this paper, the value of substrate preheating temperature is assumed in the range of $T_s \in [555.15, 591.15]$ K, i.e., $T_s/T_{\text{s,ref}} \in [0.97, 1.03]$, where $T_{\text{s,ref}} = 573.15$ K.

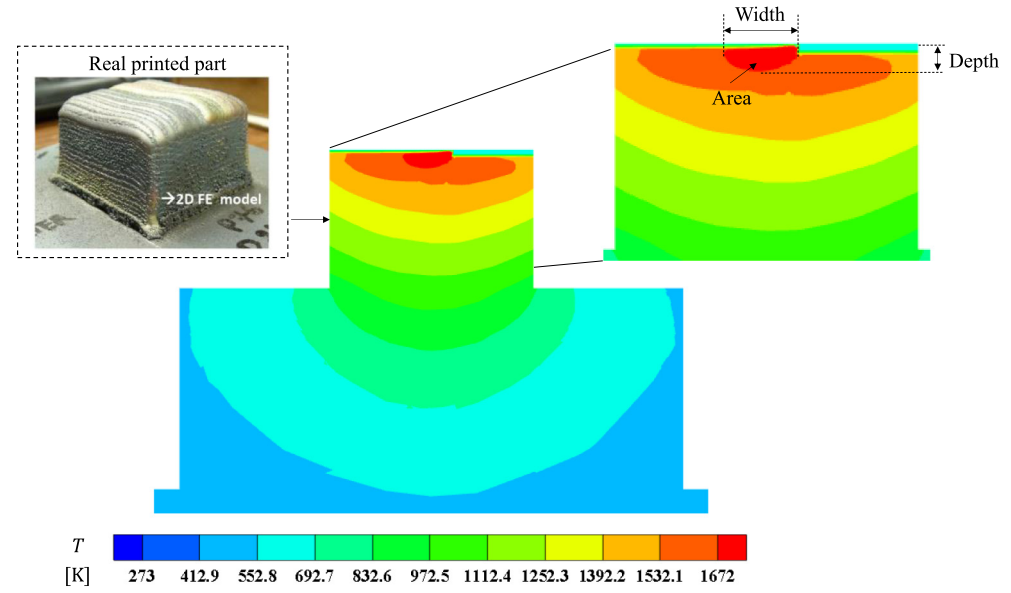

(a)

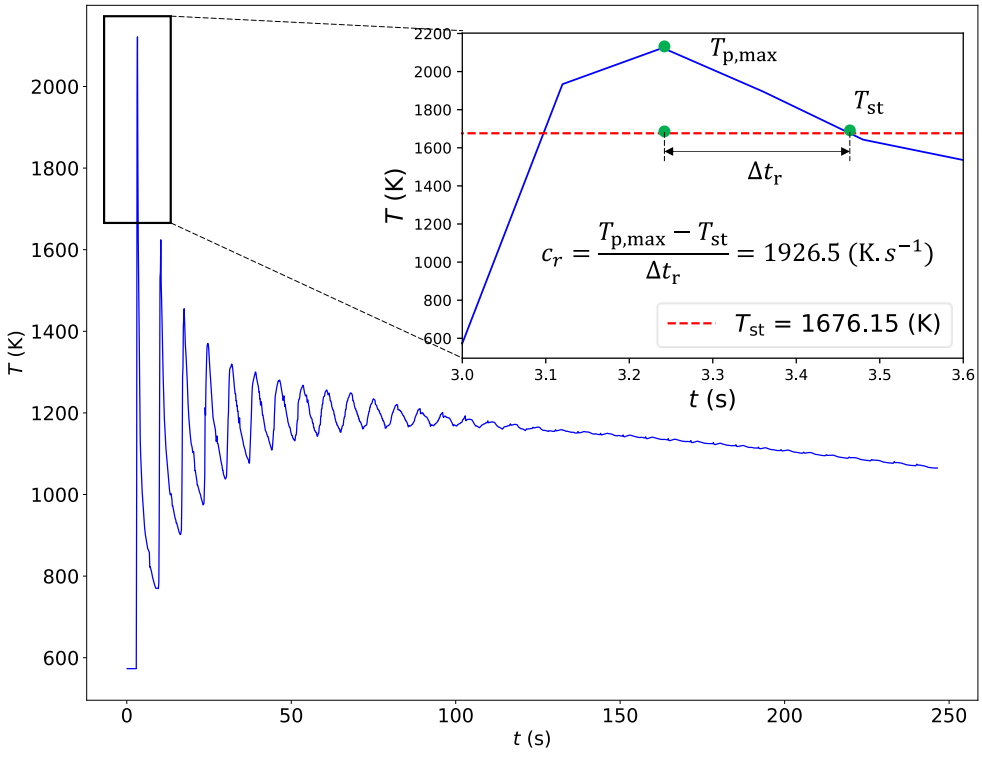

(b)

Fig. 2. A typical temperature field and melting pool sizes (depth, width, and area) (a), and the temporospatial temperature field at a random point along with the cooling rate (c_r) calculation (b) obtained by the FE simulation described in Appendix A. $T_{p,max}$ and T_{st} denote the maximum temperature at each point and the solidus temperature, respectively. Δt_r is the time-step between $T_{p,max}$ and T_{st}.

We represent uncertainty in the substrate preheating temperature by varying its reference value by ±3% ($T_a \in$ [555.15, 591.15]K).

2.2.2. Uncertain sources in material properties

The material properties that strongly influence the quality of the final fabricated product are the thermal conductivity and the heat capacity [9]. Since the precise values of these properties at high temperatures are unknown, computational models may have uncertainty due to these unknown macroscopic values. Consequently, creating a well-validated computational model of the AM processes is exceptionally challenging. Furthermore, due to rapid cooling from the melt pool in additive manufacturing processes, the materials exhibit an out-of-equilibrium refined microstructure with significantly different

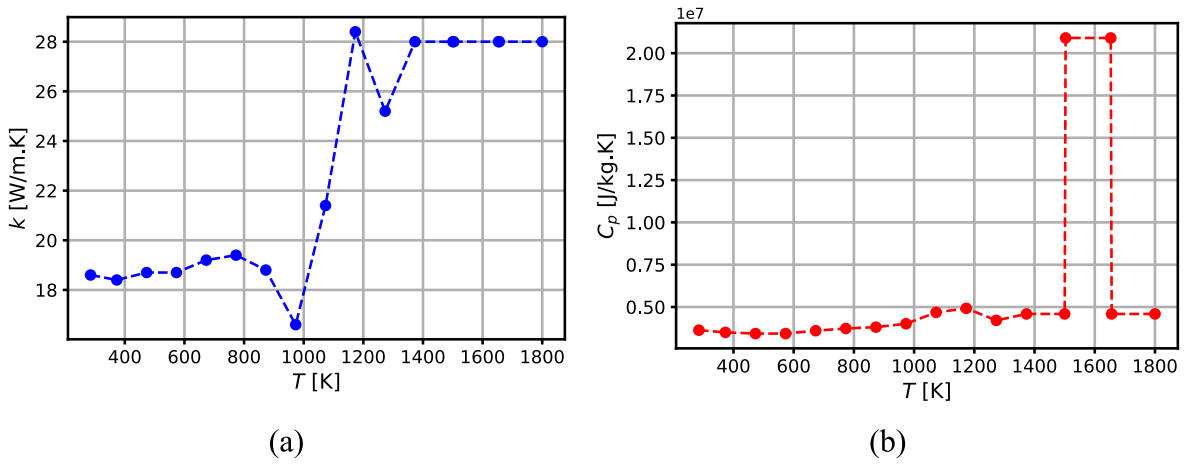

Fig. 3. Experimental measurement of thermal conductivity (a) and heat capacity (b) of the coating in the function of temperature [1].

thermo-physical properties compared to its cast counterpart at the solid-state [36]. To reduce the error on these critical material data within the FE simulations of DED process, the thermal conductivity and heat capacity were measured on samples extracted from the bulk samples generated by DED process.

(v) *Thermal conductivity*: Thermal conductivity is a quantity that determines the rate at which heat transfers through the material due to a temperature gradient. Thermal conductivity is influenced by several factors, including precipitate size and shape, precipitate distribution, precipitate morphology, inter-precipitate distance, and thermal conductivity of the matrix material and surrounding gas [1,37,38]. Fig. 3(a) shows the experimental measurement of the thermal conductivity of the M4 sample in the function of temperature. As observed in Fig. 3(a), precise determination of this quantity is challenging since it follows a non-linear behaviour.

In this paper, the value of the thermal conductivity k is in the range of [0.93, 1.07] $\times$ k_{mes}, where k_{mes} is the experimental measurement values shown in Fig. 3(a), following the technical document of the equipment (Accupyc 1340 Micromeritrics, DIL 402C Netzsch). In Section 2.3, we present the uncertainty of k by modelling the ratio $\alpha_k = (k - k_{\text{mes}})/k_{\text{mes}}$ as a uniform random variable bounded by $[-0.07, 0.07]$.

(vi) *Heat capacity*: Heat capacity is a quantity that determines the amount of heat to be supplied to a given mass of a material to produce a unit change in its temperature. The heat capacity follows a non-linear relationship with the temperature, strongly affected by the solidification phenomena, as shown in Fig. 3(b). However, due to its uncertainty in measurements and the shift of the solidus value affected by cooling and heating rate, those values are not totally reliable when modelling DED process. Also, many studies use heat capacity as a linear function of temperature [9], which significantly influences the model accuracy.

In this paper, the value of the heat capacity c_p is in the range of [0.95, 1.05] $\times$ $c_{p,\text{mes}}$, where $c_{p,\text{mes}}$ is the experimental measurement values shown in Fig. 3(b), following the technical document of the equipment (Accupyc 1340 Micromeritrics, DIL 402C Netzsch). In Section 2.3, we present the uncertainty of c_p by modelling the ratio $\alpha_c = (c_p - c_{p,\text{mes}})/c_{p,\text{mes}}$ as a uniform random variable bounded by $[-0.05, 0.05]$.

2.2.3. Uncertain sources in environmental conditions

In our study, we consider the convection and radiation emissivity of the clad as input uncertain parameters. Precisely measuring these parameters is critical in modelling the AM processes [22,39].

(vii) *Convection*: Convection is the transfer of heat by the movement of fluid between areas of different temperatures. Due to measurement uncertainty, many studies assume the convection as a forced convection instead of a natural one [36], which significantly influences the model accuracy. Also, identifying accurately the convection plays a vital role in calibrating the DED computational models, where the convection values vary with the clad height [22,39,40]. Based on our experiences and Refs. [22,40], we choose the range of convection coefficient as $h \in [200, 300]$ W/m^2 K for DED simulation.

(viii) *Radiation emissivity*: Radiation is the emission or transmission of energy through space or a material medium. Radiation is critical for accurately predicting the melting pool temperature and dimension [9] since it is strongly dependent on temperature and highly varies at elevated temperatures [41,42].

We represent the uncertainty in radiation by varying the emissivity value. As observed in [43,44], we choose the emissivity range as $\varepsilon \in [0.8, 1.0]$.

2.3. Probabilistic characterization of the uncertain sources

We adopt a probabilistic framework to quantify the impact of uncertainties on the QoIs, such as temperature field, cooling rate, and melting pool sizes. The uncertainty of input parameters discussed in Section 2.2 is expressed as intervals without further information and therefore modelled using uniform distributions in this study. We summarize the uncertainty characteristics of the input parameters in Table 1.

3. Propagation of uncertainty

This section presents the second step in our UQ study, i.e., uncertainty propagation (see Fig. 1). The uncertainty of the temperature field is modelled as a random field Y, obtained through the FE-based model as a function $f : \mathbb{R}^{11} \to \mathbb{R}$ such that

$$Y = f(\boldsymbol{q}, \boldsymbol{X}), \tag{3}$$

where

$$\boldsymbol{q} = [x, y, t] \tag{4}$$

is a multi-dimensional vector of spatial coordinates (x, y) and time (t), and $\boldsymbol{X} = [X_1, X_2, \ldots, X_8] = [\mathcal{P}, v, T_a, T_s, h, \varepsilon, \alpha_k, \alpha_c]$ contains input uncertain parameters introduced in Section 2.2 and listed in Table 1.

Several methods can be used for the uncertainty propagation, such as Monte-Carlo (MC) [14] and spectral methods [45]. In this study, the MC method is chosen owing to its simplicity. Also, the MC method does not suffer from the curse of dimensionality [15], which is for the problem with a large number of uncertain input parameters. Hereafter, we briefly describe the MC method.

3.1. Monte-Carlo method

Using the MC method, we generate n independent and identically distributed (*i.i.d.*) samples from the probability distribution function

Table 1
List of input uncertain parameters and associated uncertain ranges and distribution. For the effective laser power, the thermal conductivity, and the heat capacity, their relative values are used.

Input uncertain parameter		Notation	Mean	Minimum	Maximum	Distribution	Unit
Process parameters	Effective laser power	$\mathcal{P}$	1	0.97	1.03	Uniform	–
	Scanning speed	v	350	335	365	Uniform	mm/min
	Controllable ambient temperature	T_a	298.15	284.15	312.15	Uniform	K
	Substrate preheating temperature	T_s	573.15	555.15	591.15	Uniform	K
Material properties	Convection	h	250	200	300	Uniform	W/m^2 K
	Radiation emissivity	ε	0.9	0.8	1	Uniform	–
Environmental conditions	Thermal conductivity	α_k	1	0.93	1.07	Uniform	–
	Heat capacity	α_c	1	0.95	1.05	Uniform	–

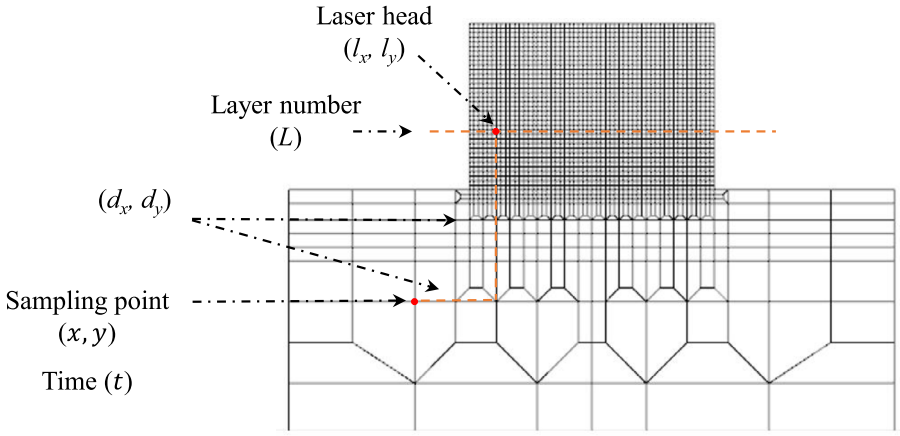

Fig. 4. The five enriched features of the FFNN-based surrogate model, evaluated at each time (t). The origin is located at the bottom left as shown in Fig. A.18.

(PDF) $\pi_{\boldsymbol{X}}$ as

$$\left\{\boldsymbol{\xi}^{(i)}, 1 \le i \le n_{\mathrm{MC}}\right\}. \tag{5}$$

The model f is then used to map each sample from $\pi_{\boldsymbol{X}}$ into the corresponding sample from π_Y such that

$$\psi^{(i)} = f(\boldsymbol{q}, \boldsymbol{\xi}^{(i)}), \tag{6}$$

to obtain the corresponding *i.i.d.* samples from π_Y as

$$\left\{\psi^{(i)}, 1 \le i \le n_{\mathrm{MC}}\right\}. \tag{7}$$

After obtaining these *i.i.d.* samples, the mean μ_Y and the variance σ_Y^2 can be approximated as

$$\mu_Y \approx \frac{1}{n_{\mathrm{MC}}} \sum_{i=1}^{n_{\mathrm{MC}}} \psi^{(i)}, \qquad \sigma_Y^2 \approx \frac{1}{n_{\mathrm{MC}}} \sum_{i=1}^{n_{\mathrm{MC}}} \left(\psi^{(i)} - \mu_Y\right)^2. \tag{8}$$

According to the central limit theorem [15], this statistical error of mean μ_Y and variance σ_Y^2 depends on the square root of the number of samples n_{MC}. In particular, the higher the number of samples n_{MC} is, the smaller the statistical error is.

Consequently, the MC method requires a large number of FE simulations f to obtain an accurate approximation, which is computationally expensive. To gain computational efficiency, we construct a DL-based surrogate model, which can be executed quickly, to replace the role of the FE model in the MC simulation.

3.2. DL-based surrogate model

Several methods can be applied to build a surrogate model, such as linear regression, polynomial regression, and feedforward neural network (FFNN) [46]. In this study, the FFNN model is chosen, owing to its advantages in approximating complex functions over high dimensional spaces, along with its reusability and the advanced hardware technologies designed for DL. Moreover, using the gradient descent method and backpropagation approach significantly reduces the computational cost of the optimization process.

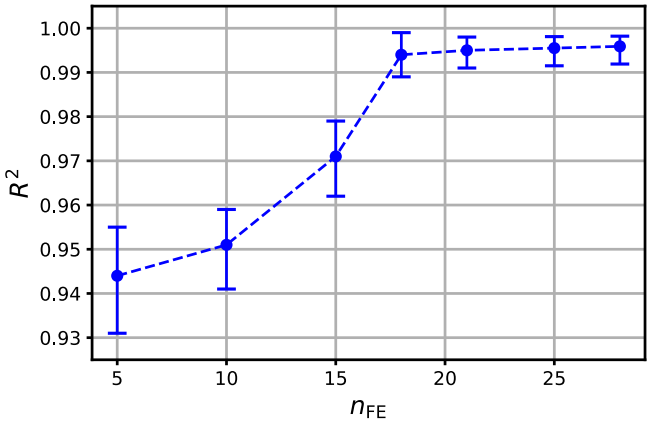

Fig. 5. The range and mean of R^2 values evaluated within data obtained from 150 FE simulations in $\boldsymbol{D}_\tau$ of FFNN-based model trained by a different n_{FE} in $\boldsymbol{D}_T$.

An FFNN-based surrogate model used to approximate the relationship between the input parameters and the temperature field has been developed in our previous study [47], which is applied for the only variation of Q_{laser}. In this study, we extend this model to account for the variation of eight input uncertain parameters as listed in Table 1. The selected architecture has four hidden layers, whose numbers of neurons are 400, 200, 200, and 100, respectively. Details of the FFNN architecture and its explainability are discussed in our previous study [47].

The FFNN-based surrogate model can be considered as a function $\hat{f}$ such that

$$\hat{f}(\boldsymbol{q}, \boldsymbol{X}|\boldsymbol{W}) \approx f(\boldsymbol{q}, \boldsymbol{X}), \tag{9}$$

where $\boldsymbol{W}$ denotes the weights and biases of the FFNN-based model.

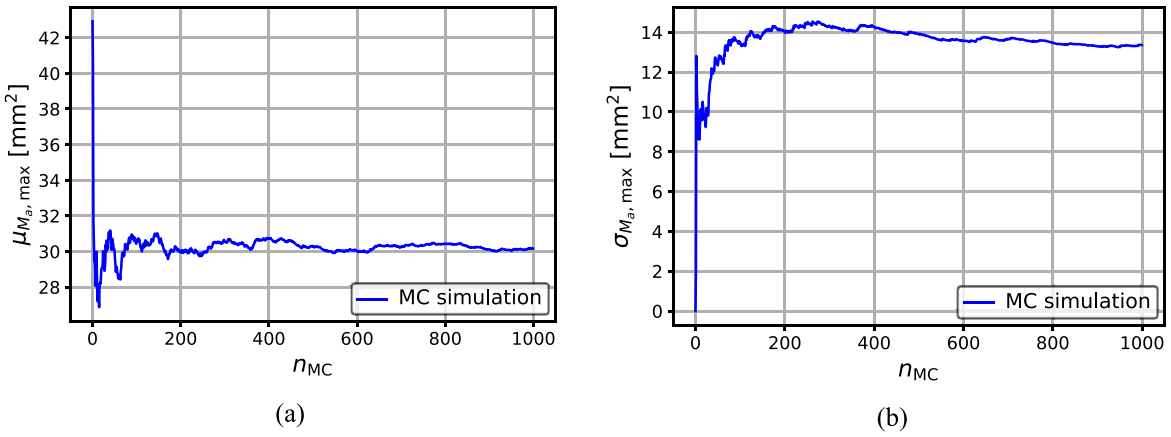

Fig. 6. The convergence of the mean (a) and standard deviation (b) of the maximum melting pool area M_a with respect to n_{MC}.

In [16], besides the four essential features, including x, y, t, and Q_{laser}, five features related to the laser position l_x, l_y, the distance from the laser position to the material point d_x, d_y, and the layer number L are used to enhance prediction accuracy. These enriched features are shown in Fig. 4.

The overall description of the enriched features can be seen in [16]. After being trained on a training dataset $\boldsymbol{D}_{\mathrm{T}}$, the FFNN model is validated on a testing dataset $\boldsymbol{D}_{\tau}$, which is independent of $\boldsymbol{D}_{\mathrm{T}}$. To assess the performance of the FFNN model, we use the metric of the coefficient of determination, known as R^2, which is widely used in DL-based applications [48]. The value of R^2, between prediction temperatures and their corresponding FE simulation data, is defined as

$$R^2 = 1 - \frac{\sum_{j=1}^{N_\tau} \left(\hat{f}\left(\boldsymbol{q}^{(j)}, \boldsymbol{X}^{(j)}\right) - T^{(j)}\right)^2}{\sum_{j=1}^{N_\tau} \left(\overline{T} - T^{(j)}\right)^2}, \quad \left(\left\{\boldsymbol{q}^{(j)}, \boldsymbol{X}^{(j)}\right\}, T^{(j)}\right) \in \boldsymbol{D}_{\tau}, \tag{10}$$

where N_τ is the size of the testing dataset and $\overline{T}$ is the mean temperature. Note that we also use R^2 metrics for subsets of prediction temperature (i.e., the maximum temperature at each time-step) and the melting pool sizes

As the FFNN-based model $\hat{f}$ has been verified to accurately replace the FE model, the MC method is mapping the characterization of the input uncertain parameters $\boldsymbol{X}$ through $\hat{f}$ to obtain the characterization of the output temperature field T. Consequently, the statistical descriptions of the temperature can be approximated as:

$$\mu_Y \approx \widehat{\mu_Y} \approx \frac{1}{n_{\mathrm{MC}}} \sum_{i=1}^{n_{\mathrm{MC}}} \hat{\psi}^{(i)}, \qquad \sigma_Y^2 \approx \left(\widehat{\sigma_Y}\right)^2 \approx \frac{1}{n_{\mathrm{MC}}} \sum_{i=1}^{n_{\mathrm{MC}}} \left(\hat{\psi}^{(i)} - \widehat{\mu_Y}\right)^2, \tag{11}$$

where $\hat{\psi}^{(i)} = \hat{f}\left(\boldsymbol{q}, \boldsymbol{\xi}^{(i)}\right)$.

4. Sensitivity analysis using variance-based method

This section presents the third step in our UQ study, i.e., sensitivity analysis (SA) (see Fig. 1). Performing the SA is a vital task of the UQ, which provides deeper knowledge about the physics of the process under investigation. For instance, based on the SA, we can identify input uncertain parameters that are significantly influential in inducing uncertainty to the final fabricated product quality. This study performs the SA using the variance-based method [23] owing to its straightforward interpretation. We perform the SA only on the melting pool size as the output for demonstrating the framework. However, this framework can be applied to other QoIs such as temperature field and cooling rate.

In our variance-based SA, the Sobol indices S_i measuring the sensitivity of the melting pool sizes (i.e., depth, width, and area) with respect to each input uncertain parameter X_i are given as

$$S_i = \frac{\sigma^2_{X_i}\left(\mathbb{E}_{\boldsymbol{X}_{\sim i}}\left(G|X_i\right)\right)}{\sigma^2(G)}, \qquad \sum_{i=1}^{8} S_i \leq 1 \tag{12}$$

Table 2
The selected training and testing datasets to build the FFNN-based model. The notation $\sim \mathcal{U}$ means sampling from the uniform distribution.

	$X_i, i = 1, \ldots, 8$	Number of FE simulations
Training ($\boldsymbol{D}_T$)	$\sim \mathcal{U}\left[\min_{X_i}, \max_{X_i}\right]$	{5, 10, 15, 18, 21, 25, 28}
Testing ($\boldsymbol{D}_\tau$)	$\sim \mathcal{U}\left[\min_{X_i}, \max_{X_i}\right]$	150

where G is a random variable represents the melting pool sizes, $\sigma^2(G)$ is the unconditional variance, $\mathbb{E}_{\boldsymbol{X}_{\sim i}}\left(G|X_i\right)$ is the expected value of G conditional on X_i (i.e., keep X_i fixed), and $\sigma^2{}_{X_i}(\mathbb{E}_{\boldsymbol{X}_{\sim i}}\left(G|X_i\right))$ is the conditional variance of G caused by a variation of X_i. The numerator term can be interpreted as the expected reduction in variance that would be obtained if keeping the parameters X_i fixed [23]. In other words, this term measures the contribution of X_i to the variance of G. The S_i takes a value between 0 and 1 because it is normalized by $\sigma^2(G)$.

By assuming the input uncertain parameters X_i are statistically independent, the higher-order effect of X_i on G (i.e., second-order) vanishes. A more detailed explanation of the theory behind the variance-based SA can be found in [23]. Based on the above discussion, $S_i = 0$ indicates that the input uncertain parameters have no impact on the variance of output and $S_i = 1$ indicates that this input uncertain parameter is the entire cause of the output variance.

5. Results and discussion

This section is organized as follows. In Section 5.1, the verification of the FFNN-based surrogate model is described. In Section 5.2, the results obtained from the uncertainty propagation study are presented. In Section 5.3, the SA to identify the input uncertain parameters that impact the melting pool sizes the most is performed. Lastly, in Section 5.4, we carry out two potential use cases to demonstrate the UQ results.

5.1. Verification of the FFNN-based surrogate model

The FFNN-based surrogate model is trained on the training dataset $\boldsymbol{D}_T$ consisted of different FE simulations (described in Appendix A) with different values of DED uncertain parameters (see Table 2). These values are obtained by sampling as a uniform distribution, reported in Table 1. In this subsection, we identify the minimum number of FE simulations required in $\boldsymbol{D}_T$ while still maintaining an acceptable accuracy of the predictability of the surrogate model.

First, we train seven independent FFNN models with the training data obtained by increasing the number of FE simulations (n_{FE}) as shown in Table 2. Fig. 5 shows the range and mean of R^2 values (see Eq. (10)) evaluated within data obtained from 150 FE simulations ($\boldsymbol{D}_\tau$)

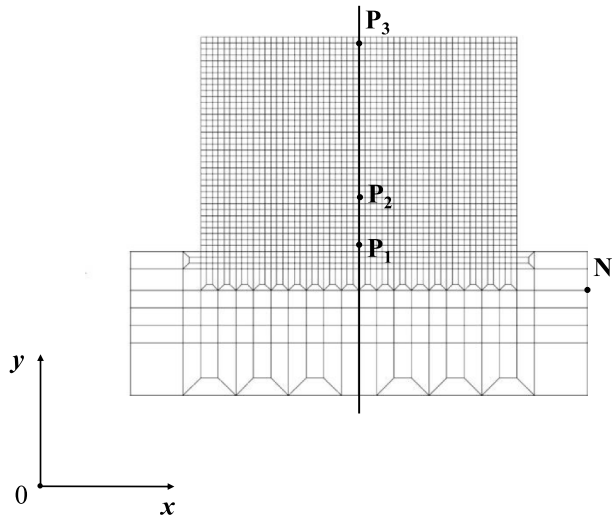

Point	x (m)	y (m)
N	0.12675	0.122
P_1	0.078	0.127764
P_2	0.0975	0.133876
P_3	0.0975	0.15374

Fig. 7. The location of four points, including three clad points (P_1, P_2, P_3) and one substrate point (N).

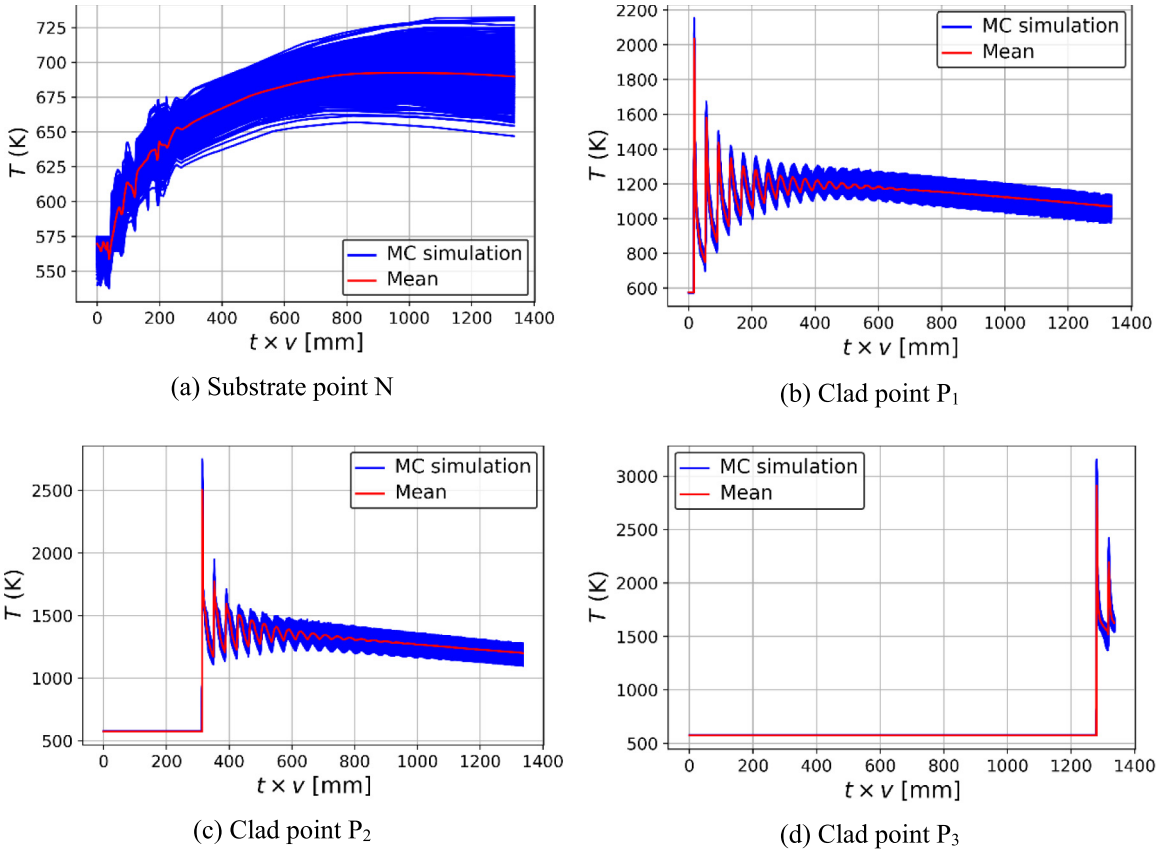

(a) Substrate point N

(b) Clad point P_1

(c) Clad point P_2

(d) Clad point P_3

Fig. 8. 1000 MC samples of the temperature evolutions of point N (a), point P_1 (b), point P_2 (c), and point P_3 (d). Note that we use the x-axis as $t \times v$, meaning the cumulative distance of the laser assuming one track per layer, to get the data in the same frequency.

of these seven surrogate models. As shown in Fig. 5, the R^2 value increases when n_{FE} increases. No significant improvement in terms of the R^2 value is observed with the $n_{\text{FE}} \geq 21$.

Second, to verify the robust performance of the FFNN model, we follow the cross-validation strategy. In particular, we create six independent FFNN models trained on the same n_{FE}, i.e., $n_{\text{FE}} = 21$ simulations, randomly chosen in the dataset. The obtained mean R^2 of the temperature field evaluated in $\boldsymbol{D}_\tau$ among the six independent models are in a range of 0.9955 and 0.9997, confirming the high accuracy of the surrogate model. We also show the temporospatial temperature fields predicted by the FE and FFNN-based surrogate models in Appendix B. In general, the FFNN-based model trained by 21 FE simulations can replace the FE model to predict the temperature history with a nearly identical accuracy in this UQ study.

5.2. Propagation of uncertainties

This section presents the results obtained by the uncertainty propagation step (see Fig. 1) discussed in Section 3. After checking the convergence analysis of MC simulation in Section 5.2.1. we show

the obtained uncertainty characteristics of the temperature field, the cooling rate, and the melting pool sizes in Sections 5.2.2, 5.2.3, and 5.2.4, respectively. Finally, we assess the computational efficiency of the FFNN model in Section 5.2.5.

5.2.1. Convergence analysis of MC simulation

As discussed in Section 3.1, the accuracy of the Monte-Carlo (MC) method depends on the number of simulations n_{MC}. Fig. 6 shows the convergence of the mean and standard deviation computed by Eq. (12) of the maximum melting pool area (i.e., the melting pool area in the last layer) with respect to the number of MC simulation n_{MC}. As observed in Fig. 6, no significant change in terms of the mean and the standard deviation are observed with $n_{MC} \geq 1000$. Therefore, we choose $n_{MC} = 1000$ to perform the MC simulation.

5.2.2. Uncertainty characteristics of the temperature field

This section investigates the obtained uncertainty characteristics of the temperature field. In particular, we examine the results at four selected points: one substrate point (N) and three clad points (P_1, P_2, and P_3) (see Fig. 7). Point P_1 is at the centre of the first printed layer and points P_2 and P_3 are located on the symmetry axis of the bulk samples, in zones that present the microstructure characteristic.

Fig. 8(a), (b), (c), and (d) show the 1000 MC samples of the temperature evolutions at four selected points N, P_1, P_2, P_3. As observed in Fig. 8, the uncertainties raised from the process parameters, material properties, and environmental conditions (see Section 2.2) lead to a substantial variation in the temperature evolutions at these four points. Particularly, the temperature evolutions vary up to 12.8% compared with their mean values in all four points. In addition, the first temperature peak at the three clad points varies up to 400 K compared to their mean value. Also, the uncertainty of the temporospatial temperature field increases with the increase of the layer number due to uncertainty accumulation (i.e., standard deviations of temperature at points N, P_1, P_2, and P_3 are up to 8%, 11.2%, 11.5%, and 12.8%, respectively, compared to their mean values).

Fig. 9(a), (b), and (c) illustrate the histograms of 1000 MC samples of the temperature at point N, point P_1, and point P_2at the moment associated at the end of each printed layer. As shown in Fig. 9, the temperature at point N tends to increase with the increase of the layer number until the 28th layer. It shows a strong influence of the heat transfer by thermal conductivity to the substrate through time. Different results are observed at the points P_1 (1st layer) and P_2 (9th layer), where the temperature first increases up to the 8th and 13th layers, respectively. After these layers, the temperature gradually decreases until the end printing time at these two points. These observations show that the heat loss due to thermal conductivity, convection, and radiation emissivity is dominant more than the heat accumulation when increasing the number of layers (i.e., the 8th layer for point P_1 and the 13th layer for point P_2). Moreover, due to the uncertainty accumulation, the standard deviation of the temperature at each point increases with the layer number. This result shows the extreme sensitivity of the temperature field to the uncertainties in the input parameters when printing a product with a high number of layers (more than eight layers).

5.2.3. Uncertainty characteristics of the cooling rate

This section shows the obtained uncertainty characteristics of the cooling rate (s_r). Moreover, we aim to confirm the influence of the clad height (H_c) with the cooling rate (i.e., the cooling rate decreases when increasing the clad height) as observed in several studies [26,49,50].

Fig. 10(a), (b), and (c) show the histogram of 1000 MC simulations of the cooling rate at the point P_1 (a), point P_2 (b), and point P_3(c), along with the FE data computed for 100 cases. The FE data are in the distribution range of the MC samples as expected. As observed in Fig. 10, a wide variation of the cooling rate is obtained at the three clad points, showing its extreme sensitivity to uncertainties in the input parameters.

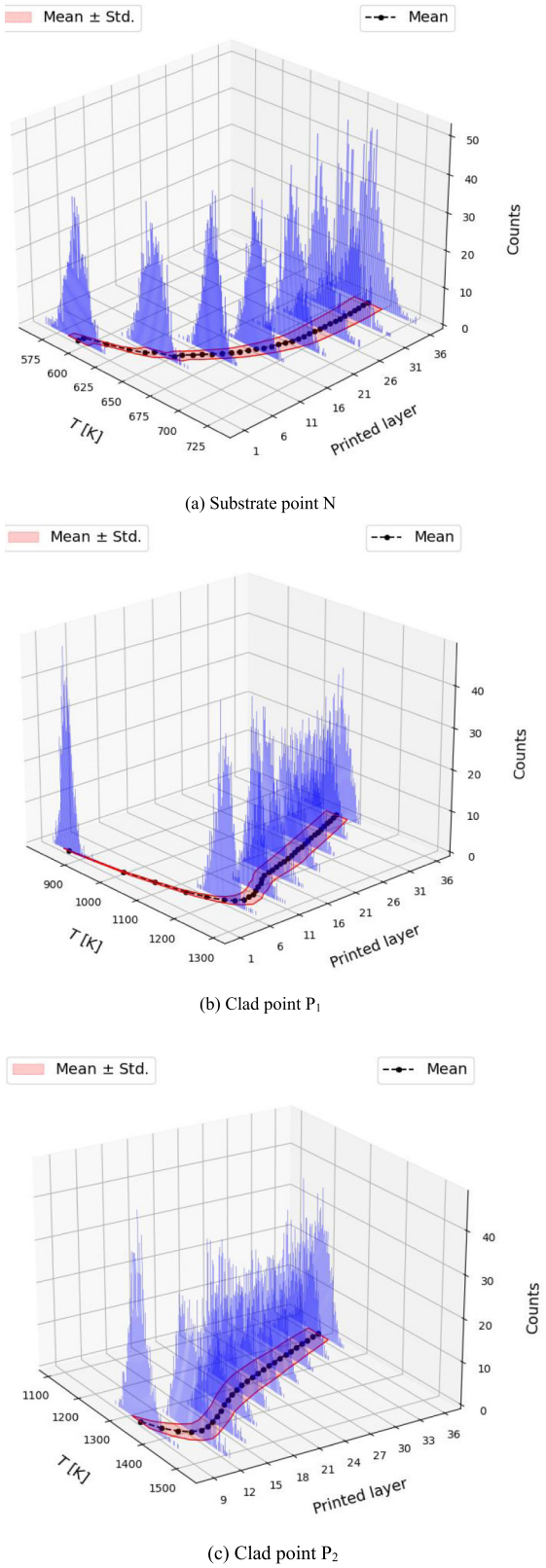

Fig. 9. Histogram of 1000 MC samples of temperature at point N (a), point P_1 (b), and point P_2 (c) at the moment associated at the end of each printed layer.

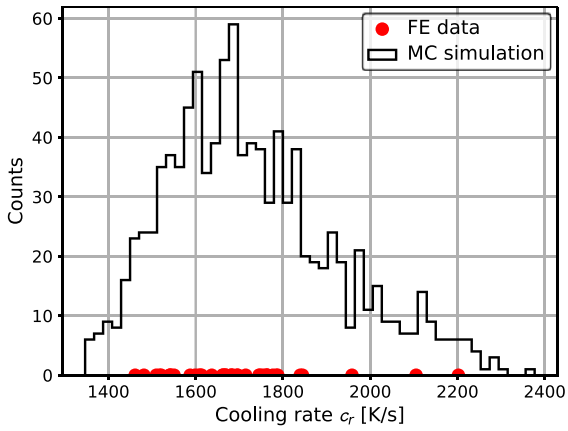

(a) Clad point P_1

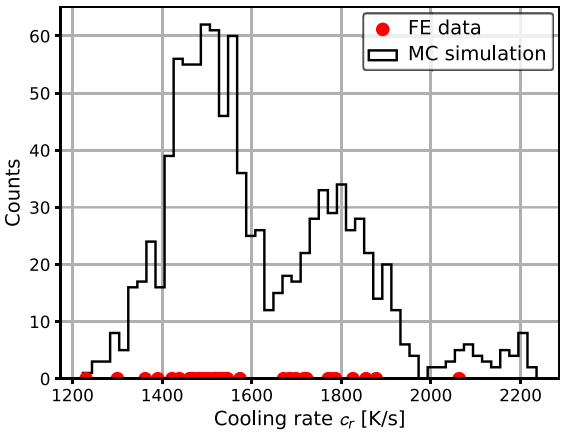

(b) Clad point P_2

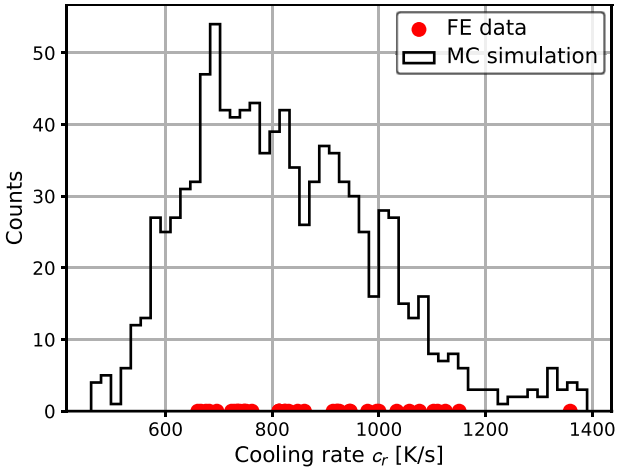

(c) Clad point P_3

Fig. 10. Histogram of 1000 MC simulations of the cooling rate at the point P_1 (a), point P_2 (b), and point P_3 (b) along with the FE data computed for 100 cases.

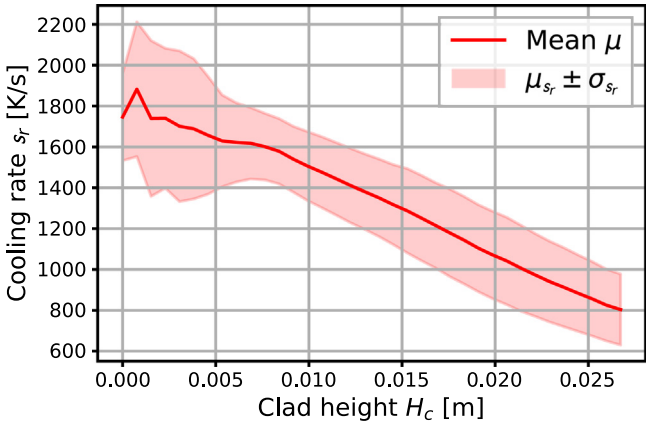

Fig. 11. The evolution of the mean cooling rate with respect to the clad height.

The interaction between the process parameters strongly varies with the clad height [26,46,47], significantly influencing the cooling rate. Fig. 11 shows the evolution of the mean cooling rate with respect to the H_c. As observed in Fig. 11, the mean gradually decreases with the H_c. For instance, the standard deviation of the cooling rate is up to 20% compared to its mean value. These results confirm the dependence of the cooling rate with the clad height H_c, which are observed in several studies [26,49,50].

5.2.4. Uncertainty propagation results of melting pool sizes

This section shows the obtained uncertainty characteristics of three geometrical characteristics of a melting pool (i.e., depth M_d, width M_w and area M_a).

Fig. 12 illustrates the empirical distribution obtained from 1000 MC simulations of the melting pool depth, width, and area located at the middle of layer. It appears that a substantial variation of the melting pool sizes is observed when increasing the layer number.

We further show the iso-values of the standard deviation of melting pool sizes in Fig. 13. The standard deviation of melting pool sizes increases with the layer number (clad height) and shows its highest value at the final printing layer. In addition, with the constant laser power for each layer, a steady melting pool cannot be reached [2]. Consequently, obtaining a steady melting pool during printing is indeed challenging for the DED process [26] (provided that the laser power is optimized and uncertainty is minimized).

In brief, the proposed framework allows quantifying the influences of the uncertainties to the temperature field, cooling rate, and melting pool sizes.

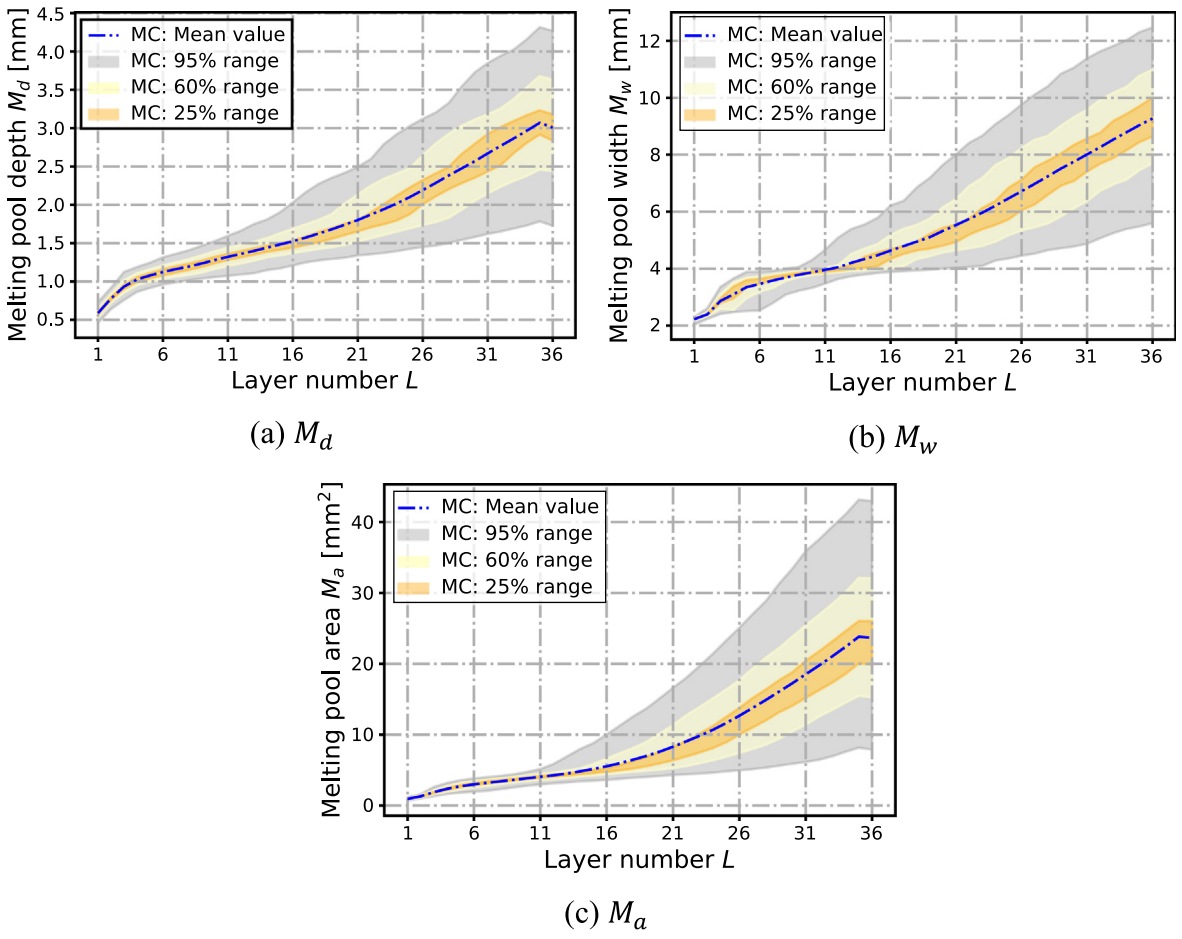

Fig. 12. Empirical distribution obtained from 1000 MC simulations of the melting pool depth (a), width (b), and area (c) located at the middle of the layer.

Table 3
Computational costs needed to perform a direct MC simulation, using the FE and FFNN-based surrogate model.

Number of MC simulations	FE model (h)	FFNN-based surrogate model (h)
1	0.6	0.0033 (12 s)
1000	600	3.3

5.2.5. Computational efficiency assessment

This section assesses the computational efficiency of the FFNN model as compared with the FE model in the uncertainty propagation step (see Fig. 1). Table 3 compares the computational cost needed to perform a direct MC simulation using the FE and FFNN-based surrogate models. A computer with the memory of 32 GB RAM, the processor of Intel i7-6700 CPU, and the GPU of NVIDIA GeForce GTX 1660 Ti was used to perform the MC simulations, FE simulations, and training of the FFNN model. For one MC simulation, the FFNN-based surrogate model only takes 12 s to compute a statistical description (i.e., mean and standard deviation) of the temperature field, which reduces 181 times as compared with the FE model. Consequently, only 3.3 h are required for 1000 MC simulations with the FFNN model, whereas using the FE model, these 1000 MC simulation would require 600 h (25 days). In summary, because the FFNN-based surrogate model requires 21 FE simulations for training, when only a few simulations are needed, there is no interest to build the surrogate model. In contrast, for uncertainty quantification or process optimization for which a large number of simulations are required, using the FFNN-based surrogate model instead of the FE model significantly reduces the computational cost in the MC simulation and would make the MC method possible.

Hereafter, we carry out the sensitivity analysis to determine which input uncertain parameter induces the most uncertainties within the output.

5.3. UQ sensitivity analysis

This section presents the results obtained by the UQ sensitivity analysis step (see Fig. 1) explained in Section 4. Hereafter, the SA using variance-based methods is performed to identify which uncertain parameters and their associated physical phenomenon are the most influential in generating uncertainty in the melting pool sizes.

Fig. 14 shows the Sobol indices for the three geometrical characteristics of the melting pool (width, depth, and area) in the final layer of the product. As observed in Fig. 14, convection, laser power, scanning speed, and thermal conductivity induce the most uncertainties within the final melting pool sizes. This result is theoretically supported because they are the main parameters controlling the heat transfer (laser power, scanning speed, and thermal conductivity) and heat loss (convection) in DED process [1,28]. The ambient temperature, the substrate preheating temperature, the radiation emissivity, and the heat capacity play a minor role in inducing uncertainties in the melting pool sizes, as they are more related to the temperature distribution in the whole bulk piece. Its global heating occurs due to thermal inertia (heat capacity) and boundary condition (ambient temperature, substrate preheating temperature, and radiation emissivity).

We further illustrate the cumulative Sobol indices measuring the sensitivity of the melting pool depth with respect to the input uncertain parameters in Fig. 15. In the first layers, the indices of the scanning speed dominate the other parameters, then they decrease until the 14th layer and become unstable until reaching the last layer. When the

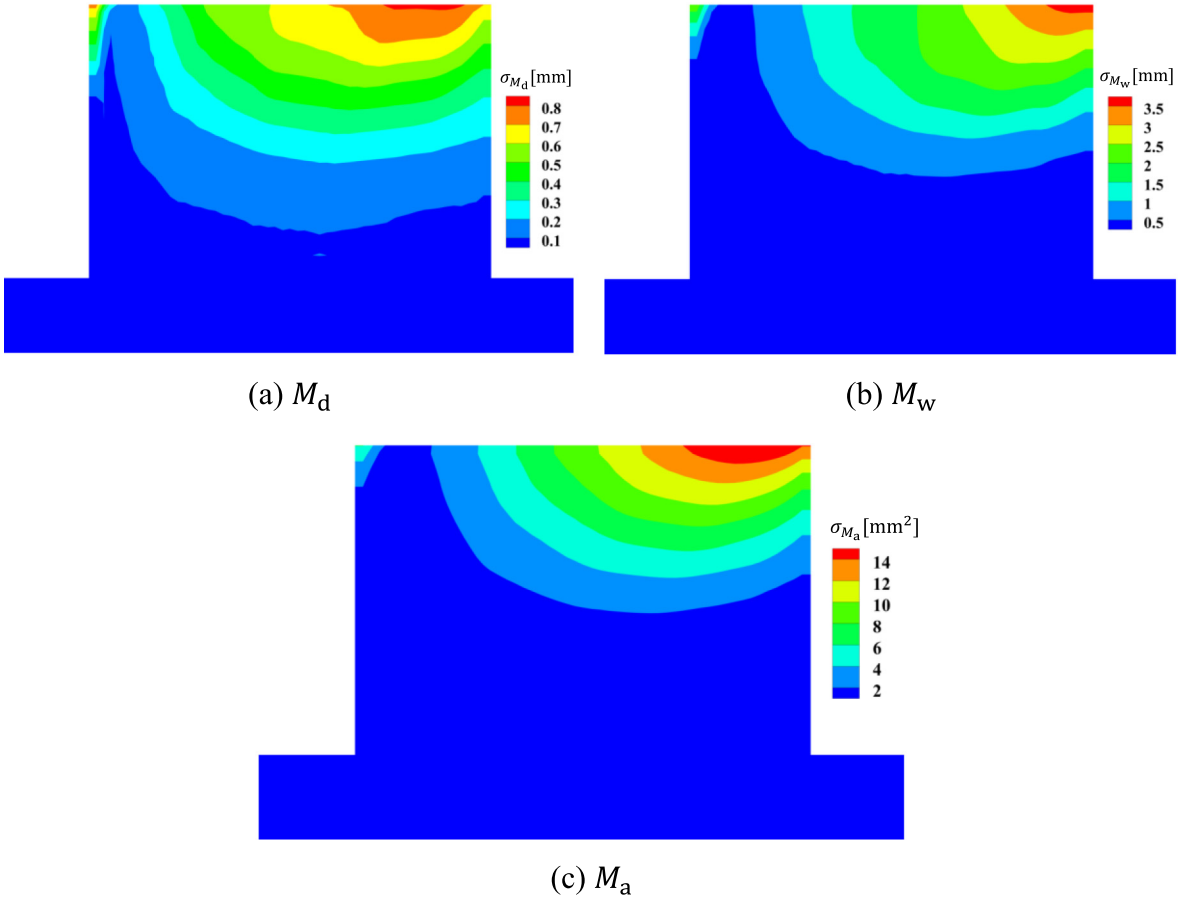

Fig. 13. The iso-values of the standard deviation of the melting pool depth (a), width (b), and area (c)

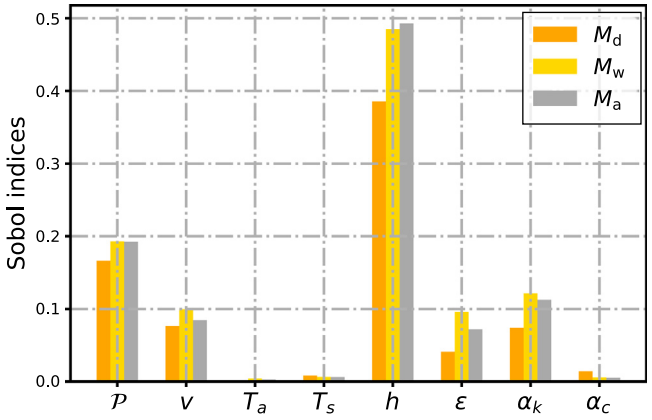

Fig. 14. The Sobol indices for each input uncertain parameter in inducing the uncertainties in the melting pool sizes on the middle point of the final layer (see Table 1 for parameter meaning).

deposition process starts, the heat transfer due to scanning speed to the bottom is dominant, while for the high layers, the heat accumulation gets more effects. In addition, convection, laser power, and thermal conductivity also play significant roles. This result highlights the most important input uncertain parameters (i.e., convection, laser power, thermal conductivity, and scanning speed) for controlling a stable melting pool. A focus on this property should be presented while optimizing the manufacturing process because it determines the microstructure genesis, which is responsible for part properties.

5.4. Potential use cases of UQ

This section introduces two potential use cases that can be further developed based on the UQ results in Sections 5.2 and 5.3. They aim at the uncertainty reduction of the cooling rate and melting pool depth by controlling four process parameters (i.e., laser power, scanning speed, ambient temperature, and substrate preheating temperature) reported in Table 1 and the four most important input uncertain parameters (i.e., laser power, scanning speed, thermal conductivity, and convection) described in Section 5.3, respectively.

5.4.1. Uncertainty reduction of the cooling rate by controlling four process parameters reported in Table 1

Because the material microstructure highly depends on the cooling rate [22,26], as discussed in Section 2.1, a process being less affected by the uncertainties raised from process parameters on the cooling rate helps to better control the DED process. However, these uncertainties are unavoidably present in a realistic printing system. Thus, a quantitative determination of their uncertain ranges that influence the cooling rate is crucial and will be assessed in this subsection.

Fig. 16 illustrates the uncertainty reduction of the cooling rate at three clad points by controlling four process parameters reported in Table 1. As observed in Fig. 16, reducing the uncertainties in these process parameters (see Section 2.2) leads to a decrease in the standard deviation of the cooling rate. An uncertainty reduction in the scanning speed appears to be the most efficient to decrease the uncertainty of the cooling rate. In contrast, the less efficient one to control is the uncertainty reduction in the ambient temperature.

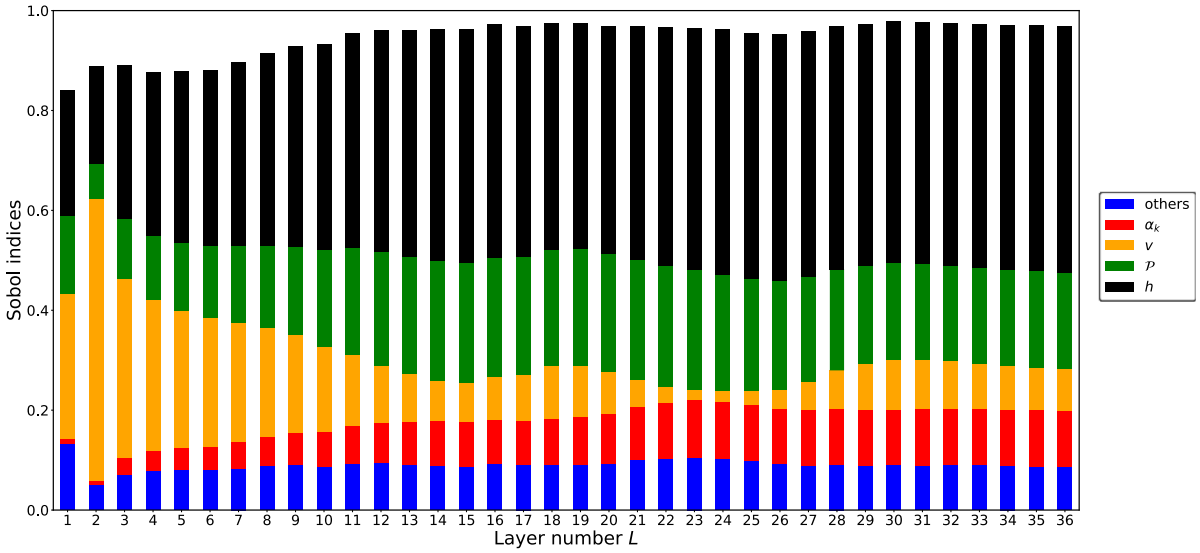

Fig. 15. Cumulative Sobol indices for each input uncertain parameter in inducing the uncertainties on the melting pool depth located at the middle of each printing layer.

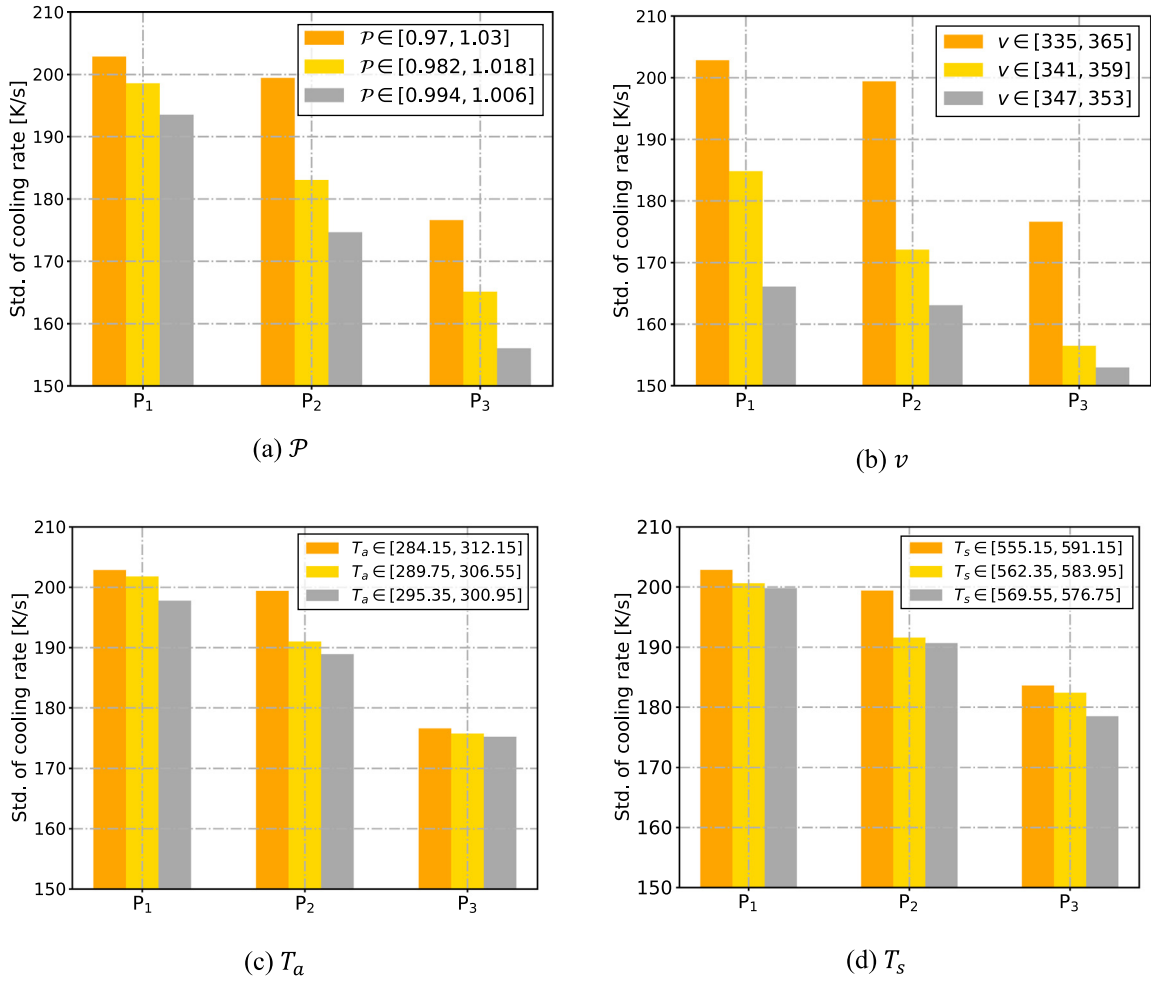

Fig. 16. The uncertainty reduction of the cooling rate at three clad points by controlling $\mathcal{P}$ (a), v (b), T_a (c), and T_s (d). Std. is the standard deviation.

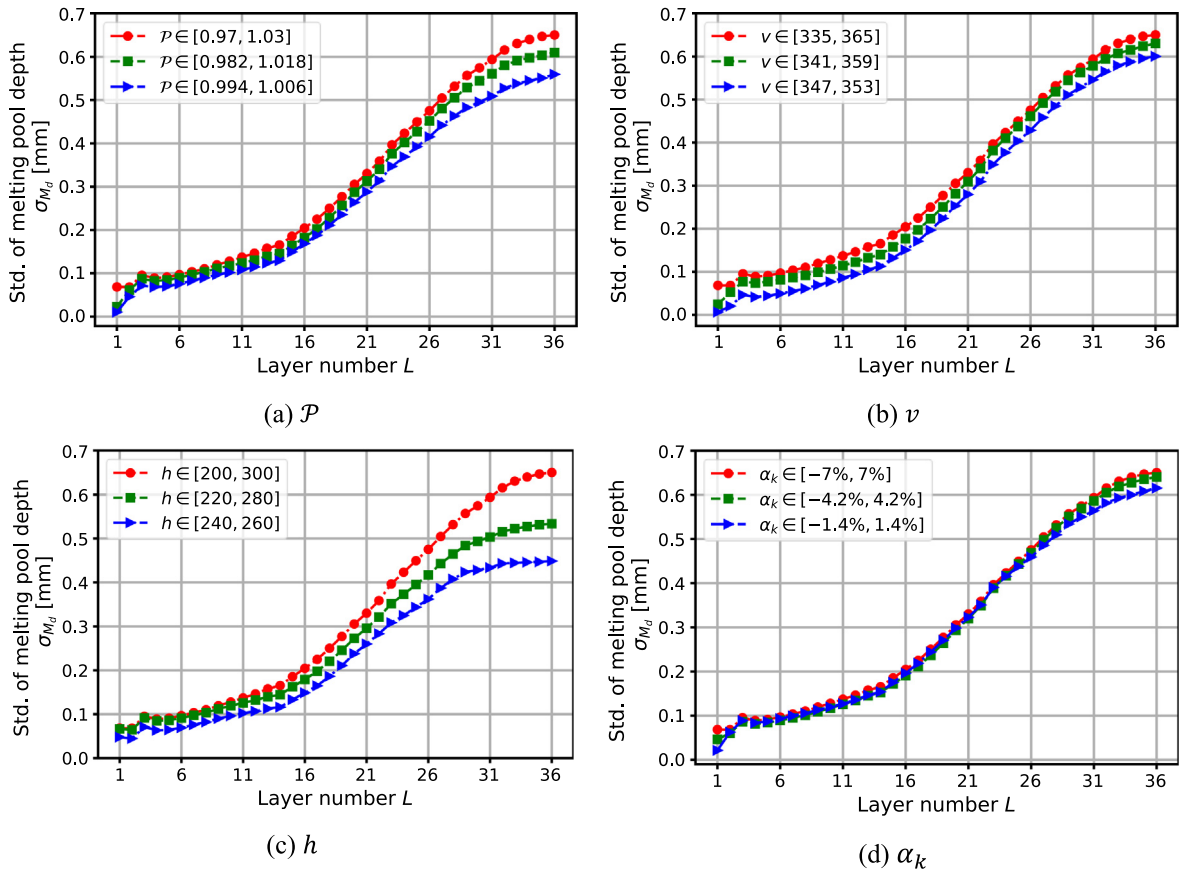

Fig. 17. The uncertainty reduction of the melting pool depth by controlling four most important input parameters, i.e., $\mathcal{P}$ (a), v (b), h (c) and α_k (d) described in Section 5.3.

5.4.2. Uncertainty reduction of the melting pool depth by controlling the four most important input parameters described in Section 5.3

A usual aim is to reduce the uncertainty in properties of the printed products (i.e., melting pool depth) related to microstructures which are responsible for mechanical properties of the final product. To this end, we must reduce the uncertainty bounds of some input sources. The results obtained from the SA have identified the important uncertain sources which should be reduced. This subsection assesses the efficiency of this approach.

Fig. 17 shows the uncertainty reduction of the melting pool depth by controlling the four most important input parameters (i.e., laser power, scanning speed, convection, and conductivity) described in Section 5.3. As observed in Fig. 17, the obtained standard deviation of the melting pool depth decreases when decreasing the uncertainty bounds of the four considered parameters. Reducing the uncertainty bound of h and $\mathcal{P}$ from 20% to 15% and 5% decreases the standard deviation of the final melting pool depth by 23% and 42%, 9.8% and 16.6%, respectively. In summary, this result suggests that the uncertainties raised in the convection and laser power should be reduced to control the melting pool depth.

6. Conclusion

In this work, the effects of uncertainties raised from the process parameters, material properties, and environmental conditions on the quality of the final printed product in DED process are quantified using the DL-based probabilistic approach. The DL-based surrogate model (FFNN model) is constructed using the offline data obtained from the FE model, which is validated by experiments (both on melting pool sizes and temperature history). The main contributions of the work are:

- Using the FFNN-based surrogate model instead of the FE model to propagate the uncertainties is shown to significantly reduce the computational cost (i.e., 3.3 h compared with 600 h for 1000 MC simulations).
- The investigated sources of uncertainty lead to a large variation of the temperature evolutions, cooling rate, and melting pool sizes like up to 12%, 20%, and 100% compared with their mean values, respectively. The effects of the uncertainties are enhanced by the number of printing layers (36 layers). Also, their mean values depend on the clad layer.
- The sensitivity analysis is carried out using the variance-based method. The results show that the convection, the laser power, the scanning speed, and the conductivity induce the most uncertainties to the melting pool sizes. A focus on these parameters should be presented to obtain stable melting pool sizes.
- Two potential use cases are assessed to demonstrate the UQ results: the uncertainty reduction of the cooling rate by controlling four process parameters and the uncertainty reduction of the melting pool sizes by controlling the four most important parameters (the one found by the SA). These use cases help to assess the efficiency of the SA and to suggest ways to improve the final printed product quality (i.e., reduce the standard deviation of the melting pool, optimize the laser power to get a steady melting pool, etc.).

As observed in this study, the AM technology inherently includes multiple sources of uncertainty that explain the observed inconsistency of the quality of the fabricated products. A DL-based optimization framework accounting for these uncertainties with significantly reduced computational cost helps to investigate UQ which in turn help to identify the sources of uncertainties that have to be carefully controlled to achieve a desired optimal printed part.

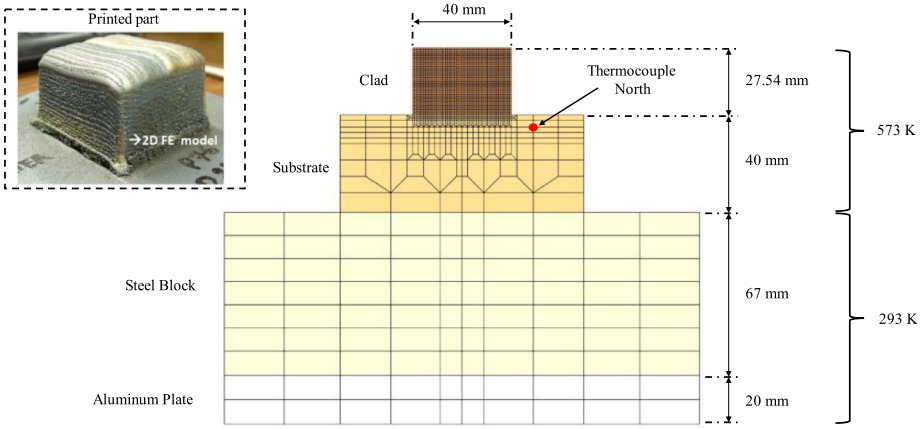

Fig. A.18. The 2D mesh and the printed part of the considered DED experiment of the M4 HSS clad sample of $40 \times 40 \times 27.54$ mm (36 layers and 27 tracks per layer). The values of 293 K and 573 K are the ambient and the substrate preheating temperatures, respectively.

Declaration of competing interest

The authors declare that they have no known competing financial interests or personal relationships that could have appeared to influence the work reported in this paper.

Acknowledgements

This work was funded by Vingroup and supported by Vingroup Innovation Foundation (VINIF) under project code **VINIF.2020.DA15.** Also, the authors would like to thank Dr. Van-Dung Nguyen and Dr. Quoc-Tuan Pham for their helpful advice on various technical issues examined in this paper.

Appendix A. DED experiment and details of the validated FE simulation

In the considered DED experiment, the laser power, nozzle scanning speed, and powder feed rate are 1100 W, 6.87 mm/s, and 76 mg/s, respectively. The preheating temperature of the 42CrMo4 substrate is 573 K, which helps avoid an early crack by reducing the temperature gradient inducing internal stress [33].

Because a 3D FE model for this sample requires a huge computational cost, we use the 2D FE model [2,40], which simulates the temperature evolutions of the middle vertical cross-section that aligns with the printing direction of the bulk sample. In 3D, the laser input energy (Q_{laser}) applied on two adjacent nodes is computed using the laser power (P) as

$$Q_{\text{laser}} = \beta \frac{2P}{\pi r_L^2},$$

where β is the absorption factor and r_L is the laser beam radius. To be representative of the 3D phenomenon, the 2D FE model uses an *effective* laser input energy ($Q_{\text{laser}} = Q_0$), where $Q_0 = 31158$ is obtained by fitting the experimental and numerical temperature evolutions.

Fig. A.18 shows the 2D FE mesh and the printed part (36 layers) of the considered DED experiment. More technical details of the FE model, including the experimental set-up, numerical solver, and mesh strategy, can be found in [2].

Fig. A.19 shows the temperature evolutions at thermocouple North (see Fig. A.18), obtained from the experiment and the FE predictions, showing a good agreement. Therefore, the FE model to compute the temperature field can be considered validated versus the available experimental results and will be used to generate the database for the DL model.

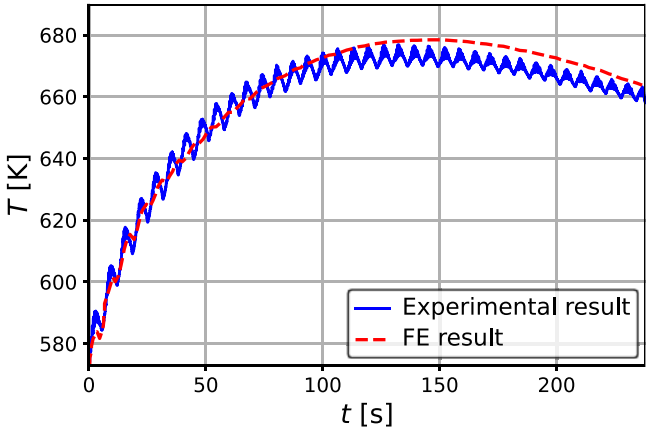

Fig. A.19. Temperature evolutions at thermocouple North obtained from the experiment and the FE model.

In addition, the global prediction of the measured temperature evolution shown in Fig. A.19 is only a first validation. A second one is the predicted melt pool size in agreement with the measured one and a third one is the explanation of the microstructure heterogeneity (nature, shape and size of the precipitations) thanks to the different thermal histories predicted along the sample height.

Appendix B. Temporospatial temperature field prediction

This appendix illustrates the temporospatial temperature field and melting pool area in a random dataset from $\boldsymbol{D}_\tau$ predicted by the FFNN-based and FE models. As observed in Fig. B.20, the predicted temporospatial temperature field is in good agreement between the FFNN-based and FE models. At each point, the temperature profiles show cyclic heating–cooling waves (also called temperature oscillations). The peaks and the oscillations are well captured by the FFNN-based model, ensuring an excellent predictive surrogate model.

Fig. B.21depicts the melting pool area located at the middle layer in a random dataset from $\boldsymbol{D}_\tau$ predicted by the FFNN-based and FE models. As shown in Fig. B.21, the melting pool area computed via the FFNN-based model is in line with that via the FE model.

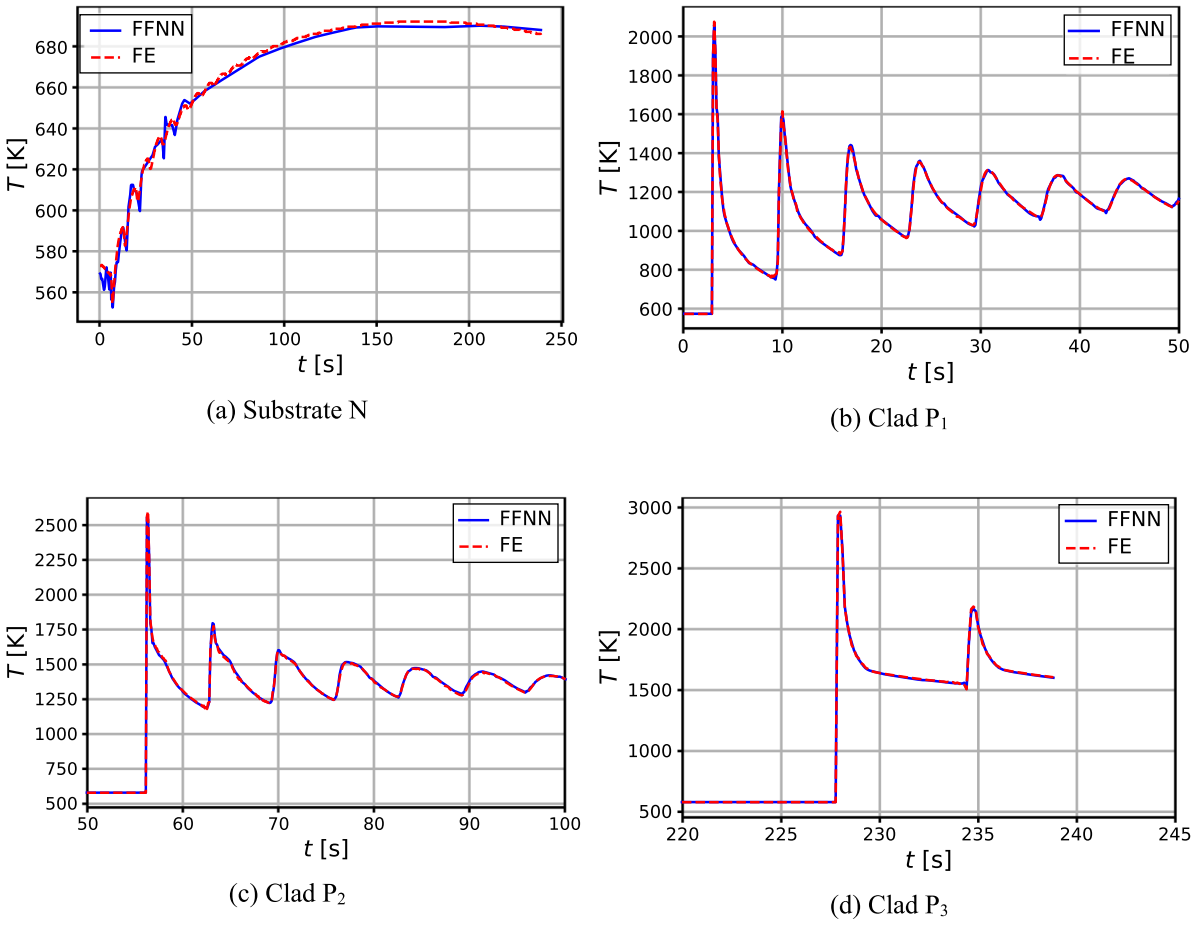

Fig. B.20. The temperature evolutions at four points predicted by the FFNN-based and FE models in a random dataset from $\boldsymbol{D}_\tau$.

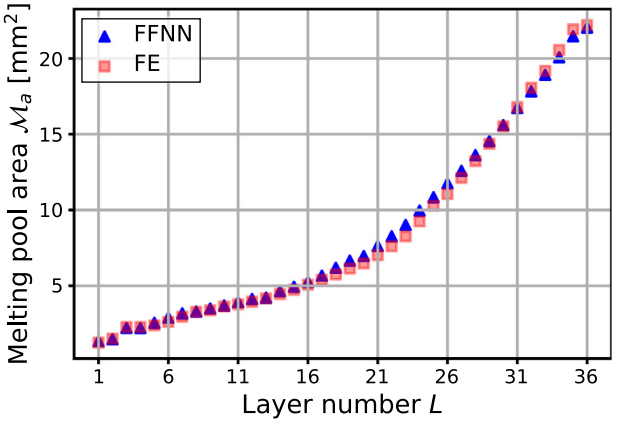

Fig. B.21. The melting pool area located at the middle layer predicted by the FFNN-based and FE models in a random dataset from $\boldsymbol{D}_\tau$.

References

[1] R.T. Jardin, V. Tuninetti, J.T. Tchuindjang, N. Hashemi, R. Carrus, A. Mertens, L. Duchêne, H.S. Tran, A.M. Habraken, Sensitivity analysis in the modeling of a high-speed, steel, thin wall produced by directed energy deposition, Metals 10 (2020) http://dx.doi.org/10.3390/met10111554.

[2] R.T. Jardin, J. Tchoufang Tchuindjang, L. Duchêne, H.S. Tran, N. Hashemi, R. Carrus, A. Mertens, A.M. Habraken, Thermal histories and microstructures in direct energy deposition of a high speed steel thick deposit, Mater. Lett. 236 (2019) http://dx.doi.org/10.1016/j.matlet.2018.09.157.

[3] Y.C. Shin, N. Bailey, C. Katinas, W. Tan, Predictive modeling capabilities from incident powder and laser to mechanical properties for laser directed energy deposition, Comput. Mech. 61 (2018) http://dx.doi.org/10.1007/s00466-018-1545-1.

[4] A.J. Pinkerton, W. Ul Haq Syed, L. Li, An experimental and theoretical investigation of combined gas- and water-atomized powder deposition with a diode laser, J. Laser Appl. 18 (2006) http://dx.doi.org/10.2351/1.2164486.

[5] J. Mazumder, D. Dutta, N. Kikuchi, A. Ghosh, Closed loop direct metal deposition: Art to part, Opt.Lasers Eng.. 34 (2000) http://dx.doi.org/10.1016/S0143-8166(00)00072-5.

[6] D.G. Ahn, Applications of laser assisted metal rapid tooling process to manufacture of molding & forming tools - state of the art, Int. J. Precis. Eng. Manuf. 12 (2011) http://dx.doi.org/10.1007/s12541-011-0125-5.

[7] D.G. Ahn, Direct metal additive manufacturing processes and their sustainable applications for green technology: A review, Int. J. Precis. Eng. Manuf. - Green Technol. 3 (2016) http://dx.doi.org/10.1007/s40684-016-0048-9.

[8] P. Nath, Z. Hu, S. Mahadevan, Uncertainty quantification of grain morphology in laser direct metal deposition, Model. Simul. Mater. Sci. Eng. 27 (2019) http://dx.doi.org/10.1088/1361-651X/ab1676.

[9] T. Moges, G. Ameta, P. Witherell, A review of model inaccuracy and parameter uncertainty in laser powder bed fusion models and simulations, J. Manuf. Sci. Eng. Trans. ASME 141 (2019) http://dx.doi.org/10.1115/1.4042789.

[10] Z. Wang, C. Jiang, P. Liu, W. Yang, Y. Zhao, M.F. Horstemeyer, L.Q. Chen, Z. Hu, L. Chen, Uncertainty quantification and reduction in metal additive manufacturing, Npj Comput. Mater. 6 (2020) http://dx.doi.org/10.1038/s41524-020-00444-x.

[11] Z. Hu, S. Mahadevan, Uncertainty quantification and management in additive manufacturing: current status, needs, and opportunities, Int. J. Adv. Manuf. Technol. 93 (2017) http://dx.doi.org/10.1007/s00170-017-0703-5.

[12] Z. Hu, S. Mahadevan, Uncertainty quantification in prediction of material properties during additive manufacturing, Scr. Mater. 135 (2017) http://dx.doi.org/10.1016/j.scriptamat.2016.10.014.

[13] P. Nath, Z. Hu, S. Mahadevan, Multi-level uncertainty quantification in additive manufacturing, in: Solid Freeform Fabrication 2017: Proceedings of the 28th Annual International Solid Freeform Fabrication Symposium - an Additive Manufacturing Conference, SFF 2017, 2020.

[14] T. v. Hoang, L. Wu, S. Paquay, J.C. Golinval, M. Arnst, L. Noels, A computational stochastic multiscale methodology for MEMS structures involving adhesive contact, Tribol. Int. 110 (2017) http://dx.doi.org/10.1016/j.triboint.2016.10.007.

[15] M. Arnst, J.P. Ponthot, An overview of nonintrusive characterization, propagation, and sensitivity analysis of uncertainties in computational mechanics, Int. J. Uncertain. Quantif. 4 (2014) http://dx.doi.org/10.1615/Int.J.UncertaintyQuantification.2014006990.

[16] T.Q.D. Pham, T.-V. Hoang, T.Q. Pham, P.T. Huyng, X.V. Tran, S. Fetni, L. Duchêne, H.S. Tran, A.M. Habraken, Data-driven prediction of temperature evolution in metallic additive manufacturing process, in: ESAFORM 2021, 2021, http://dx.doi.org/10.25518/esaform21.2599.

[17] M. Mozaffar, A. Paul, R. Al-Bahrani, S. Wolff, A. Choudhary, A. Agrawal, K. Ehmann, J. Cao, Data-driven prediction of the high-dimensional thermal history in directed energy deposition processes via recurrent neural networks, Manuf. Lett. 18 (2018) http://dx.doi.org/10.1016/j.mfglet.2018.10.002.

[18] M. Roy, O. Wodo, Data-driven modeling of thermal history in additive manufacturing, Addit. Manuf. 32 (2020) http://dx.doi.org/10.1016/j.addma.2019.101017.

[19] F. Lopez, P. Witherell, B. Lane, Identifying uncertainty in laser powder bed fusion additive manufacturing models, J. Mech. Des. Trans. ASME 138 (2016) http://dx.doi.org/10.1115/1.4034103.

[20] G. Tapia, W. King, L. Johnson, R. Arroyave, I. Karaman, A. Elwany, Uncertainty propagation analysis of computational models in laser powder bed fusion additive manufacturing using polynomial chaos expansions, J. Manuf. Sci. Eng. Trans. ASME 140 (2018) http://dx.doi.org/10.1115/1.4041179.

[21] J.A.T. Sudarsanam, S. Babu, Through Collaboration, Advanced simulation for additive manufacturing: Meeting challenges, 2015, http://www.osti.gov/scitech/.

[22] H.S. Tran, J.T. Tchuindjang, H. Paydas, A. Mertens, R.T. Jardin, L. Duchêne, R. Carrus, J. Lecomte-Beckers, A.M. Habraken, 3D thermal finite element analysis of laser cladding processed Ti-6al-4V part with microstructural correlations, Mater. Des. 128 (2017) http://dx.doi.org/10.1016/j.matdes.2017.04.092.

[23] A. Saltelli, P. Annoni, I. Azzini, F. Campolongo, M. Ratto, S. Tarantola, Variance based sensitivity analysis of model output, design and estimator for the total sensitivity index, Comput. Phys. Comm. 181 (2010) http://dx.doi.org/10.1016/j.cpc.2009.09.018.

[24] D.A. Anderson, J.C. Tannehill, R.H. Pletcher, Computational fluid mechanics and heat transfer, 1984.

[25] S. Mosayebidorcheh, D.D. Ganji, M. Farzinpoor, Approximate solution of the nonlinear heat transfer equation of a fin with the power-law temperature-dependent thermal conductivity and heat transfer coefficient, Propuls. Power Res. 3 (2014) http://dx.doi.org/10.1016/j.jppr.2014.01.005.

[26] J.L. Bennett, S.J. Wolff, G. Hyatt, K. Ehmann, J. Cao, Thermal effect on clad dimension for laser deposited inconel 718, J. Manuf. Process. 28 (2017) http://dx.doi.org/10.1016/j.jmapro.2017.04.024.

[27] W.E. King, H.D. Barth, V.M. Castillo, G.F. Gallegos, J.W. Gibbs, D.E. Hahn, C. Kamath, A.M. Rubenchik, Observation of keyhole-mode laser melting in laser powder-bed fusion additive manufacturing, J. Mater. Process. Technol. 214 (2014) http://dx.doi.org/10.1016/j.jmatprotec.2014.06.005.

[28] L.E. Criales, Y.M. Arısoy, T. Özel, Sensitivity analysis of material and process parameters in finite element modeling of selective laser melting of Inconel 625, Int. J. Adv. Manuf. Technol. 86 (2016) http://dx.doi.org/10.1007/s00170-015-8329-y.

[29] in: Proceedings - ASPE 2014 Spring Topical Meeting: Dimensional Accuracy and Surface Finish in Additive Manufacturing, Proceedings - ASPE 2014 Spring Topical Meeting: Dimensional Accuracy and Surface Finish in Additive Manufacturing. (2014).

[30] H. Yeung, J. Neira, B. Lane, J. Fox, F. Lopez, Laser path planning and power control strategies for powder, in: Proceedings of the Solid Freeform Fabrication Symposium, 2016.

[31] B.G. Compton, B.K. Post, C.E. Duty, L. Love, V. Kunc, Thermal analysis of additive manufacturing of large-scale thermoplastic polymer composites, Addit. Manuf. 17 (2017) http://dx.doi.org/10.1016/j.addma.2017.07.006.

[32] L. Fang, Y. Yan, O. Agarwal, S.H. Kang, S. Yao, J.E. Seppala, Effects of environmental temperature and humidity on the geometry and strength of polycarbonate specimens prepared by fused filament fabrication, Materials 13 (2020) http://dx.doi.org/10.3390/ma13194414.

[33] K. Kempen, B. Vrancken, S. Buls, L. Thijs, J. van Humbeeck, J.P. Kruth, Selective laser melting of crack-free high density M2 high speed steel parts by baseplate preheating, J. Manuf. Sci. Eng. Trans. ASME 136 (2014) http://dx.doi.org/10.1115/1.4028513.

[34] C.Y. Huang, K. Srihari, P. Børgesen, Optimization of the substrate preheat temperature for the encapsulation of flip chip devices, Int. J. Adv. Manuf. Technol. 16 (2000) http://dx.doi.org/10.1007/PL00013134.

[35] D. Tang, Effect of substrate preheating temperature and coating thickness on residual stress in plasma sprayed hydroxyapatite coating, IOP Conf. Ser.: Mater. Sci. Eng. (2015) http://dx.doi.org/10.1088/1757-899X/87/1/012097.

[36] E. Strumza, O. Yeheskel, S. Hayun, The effect of texture on the anisotropy of thermophysical properties of additively manufactured AlSi10Mg, Addit. Manuf. 29 (2019) http://dx.doi.org/10.1016/j.addma.2019.06.013.

[37] M.R. Alkahari, T. Furumoto, T. Ueda, A. Hosokawa, R. Tanaka, M.S. Abdul Aziz, Thermal conductivity of metal powder and consolidated material fabricated via selective laser melting, Key Eng. Mater. (2012) http://dx.doi.org/10.4028/www.scientific.net/KEM.523-524.244.

[38] M. Rombouts, L. Froyen, A. v. Gusarov, E.H. Bentefour, C. Glorieux, Photopyroelectric measurement of thermal conductivity of metallic powders, J. Appl. Phys. 97 (2005) http://dx.doi.org/10.1063/1.1832740.

[39] J.C. Heigel, P. Michaleris, E.W. Reutzel, Thermo-mechanical model development and validation of directed energy deposition additive manufacturing of Ti-6Al-4V, Addit. Manuf. 5 (2015) http://dx.doi.org/10.1016/j.addma.2014.10.003.

[40] S. Fetni, T.M. Enrici, T. Niccolini, H.S. Tran, O. Dedry, L. Duchêne, A. Mertens, A.M. Habraken, Thermal model for the directed energy deposition of composite coatings of 316l stainless steel enriched with tungsten carbides, Mater. Des. 204 (2021) http://dx.doi.org/10.1016/j.matdes.2021.109661.

[41] P. Kieruj, D. Przestacki, T. Chwalczuk, Determination of emissivity coefficient of heat-resistant super alloys and cemented carbide, Arch. Mech. Technol. Mater. 36 (2016) http://dx.doi.org/10.1515/amtm-2016-0006.

[42] S.S. Sih, J.W. Barlow, Emissivity of powder beds, in: The 6th Solid Freeform Fabrication Symposium, 1995.

[43] S. Fetni, T.M. Enrici, T. Niccolini, H.S. Tran, O. Dedry, L. Duchêne, A. Mertens, A.M. Habraken, Thermal model for the directed energy deposition of composite coatings of 316l stainless steel enriched with tungsten carbides, Mater. Des. 204 (2021) http://dx.doi.org/10.1016/j.matdes.2021.109661.

[44] F. Valiorgue, A. Brosse, P. Naisson, J. Rech, H. Hamdi, J.M. Bergheau, Emissivity calibration for temperatures measurement using thermography in the context of machining, Appl. Therm. Eng. 58 (2013) http://dx.doi.org/10.1016/j.applthermaleng.2013.03.051.

[45] B. Sudret, Uncertainty propagation and sensitivity analysis in mechanical models – Contributions to structural reliability and stochastic spectral methods, _Habilitation (2007).

[46] G. bin Huang, Q.Y. Zhu, C.K. Siew, Extreme learning machine: Theory and applications, Neurocomputing 70 (2006) http://dx.doi.org/10.1016/j.neucom.2005.12.126.

[47] T.Q.D. Pham, T.V. Hoang, X. van Tran, Q.T. Pham, S. Fetni, L. Duchêne, H.S. Tran, A.-M. Habraken, Fast and accurate prediction of temperature evolutions in additive manufacturing process using deep learning, J. Intell. Manuf. (2022) http://dx.doi.org/10.1007/s10845-021-01896-8.

[48] N.J.D. Nagelkerke, A note on a general definition of the coefficient of determination, Biometrika 78 (1991) http://dx.doi.org/10.1093/biomet/78.3.691.

[49] Q. li Zhang, J. hua Yao, J. Mazumder, Laser direct metal deposition technology and microstructure and composition segregation of inconel 718 superalloy, J. Iron Steel Res. Int. 18 (2011) http://dx.doi.org/10.1016/S1006-706X(11)60054-X.

[50] S. Ji, F. Liu, T. Shi, G. Fu, S. Shi, Effects of defocus distance on three-beam laser internal coaxial wire cladding, Chinese J. Mech. Eng. 34 (2021) 45, http://dx.doi.org/10.1186/s10033-021-00560-9.